Materials Today Communications 51 (2026) 114898

Contents lists available at ScienceDirect

Materials Today Communications

journal homepage: www.elsevier.com/locate/mtcomm

Structure, nanostructure and unconventional magnetic state of the light rare-earths based $Ce_xPrNdSm$ ($x = 0.01–1.5$) medium-entropy alloys

Julia Petrović [a], Stanislav Vrtnik [a,b], Andreja Jelen [a], Primož Koželj [a,b], Jože Luzar [a], Peter Mihor [a], Gregor Kapun [c,d], Goran Dražić [a,c], Anton Meden [e], Pascal Boulet [f,*], Janez Dolinšek [a,b,**]

[a] Jozef Stefan Institute, Jamova 39, Ljubljana, SI 1000, Slovenia
[b] University of Ljubljana, Faculty of Mathematics and Physics, Jadranska 19, Ljubljana, SI 1000, Slovenia
[c] National Institute of Chemistry, Hajdrihova 19, Ljubljana, SI 1000, Slovenia
[d] Center of Excellence on Nanoscience and Nanotechnology – Nanocenter, Jamova 39, Ljubljana, SI 1000, Slovenia
[e] University of Ljubljana, Faculty of Chemistry and Chemical Technology, Večna pot 113, Ljubljana, SI 1000, Slovenia
[f] Institut Jean Lamour, UMR 7198 CNRS – Université de Lorraine, Campus Artem, 2 allée André Guinier, BP 50840, Nancy F-54011, France

ARTICLE INFO

Keywords:
High-entropy alloys
Light rare earths
Nanostructured materials
Unconventional magnetic state

ABSTRACT

We present a study of structure, microstructure, nanostructure and magnetic state of the $Ce_xPrNdSm$ ($x = 0.01–1.5$) medium-entropy alloys composed of the light rare earths only. Magnetic light rare earths are fundamentally different from the heavy ones, because the crystal-field interaction in the former is able to reduce or completely destroy the ionic magnetic moments at low temperatures. The alloys crystallize in a double hexagonal close-packed structure in the form of a single-phase nanostructured solid solution. The low-temperature magnetic state is inhomogeneous, being a mixture of paramagnetic domains appearing in the crystal regions with larger destruction of the moments and spin glass (SG)-type spin domains in the regions with less destructed moments. Such mixed state is intrinsic and specific to the light-lanthanide multi-component solid solutions. The SG-type domains are magnetically frustrated spin entities with broken ergodicity below the spin freezing temperature T_f. In the low-Ce content alloys, the SG-type domains resemble canonical SGs, while in the Ce-concentrated alloys, some ferrimagnetically ordered clusters with nonzero spontaneous magnetization have formed additionally. The increased Ce content x continuously reduces the average exchange coupling, as evidenced from the shift of T_f towards lower temperatures and the speed-up of spin dynamics into the direction of superparamagnets.

1. Introduction

Searching for novel high-entropy alloys (HEAs) with nontrivial magnetic structures, mixing of the rare-earth (RE) elements offers attractive possibilities. Great similarity of the RE elements' chemical properties allows their almost complete mutual solubility on a crystal lattice, while random distribution of the elements with disparate magnetic properties can result in unprecedented magnetic structures. HEAs based on the RE elements from the heavy half of the lanthanide series (from Gd to Lu), and including the light lanthanide Ce, have already been investigated in the past [1–14]. Pure metals of the heavy REs are considered well understood, both experimentally and theoretically [15]. The metals crystallize in the hexagonal close-packed (hcp) lattice (with the exception of Yb, which is face-centered cubic – fcc) and exhibit a plethora of magnetically ordered structures, both ferromagnetic (FM) and antiferromagnetic (AFM). The latter include modulated AFM phases with magnetic moments arranged either helically in the hcp basal plane, conically or as a longitudinal wave along the hexagonal direction, with the modulation wavelength either commensurate or incommensurate with the crystal lattice. Theoretically, bulk magnetic structures of the RE metals can be adequately described by the mean-field Hamiltonian containing three terms: (*i*) indirect exchange between the localized RE moments via the conduction electrons (the Ruderman-Kittel-Kazuya-Yosida – RKKY interaction), (*ii*) crystal-field (CF) term describing the electrostatic interaction between the anisotropic 4*f* electron orbital and the crystalline electric fields from the

* Corresponding author.
** Corresponding author at: Jozef Stefan Institute, Jamova 39, Ljubljana, SI 1000, Slovenia.
E-mail addresses: p.boulet@univ-lorraine.fr (P. Boulet), jani.dolinsek@ijs.si (J. Dolinšek).

https://doi.org/10.1016/j.mtcomm.2026.114898
Received 5 January 2026; Received in revised form 17 February 2026; Accepted 20 February 2026
Available online 20 February 2026

neighboring ionic and electronic charges and (*iii*) Zeeman interaction of the moments with the external magnetic field. Most magnetic structures found in the heavy-RE metals can be accounted for by recognizing the dominant role of the exchange, and considering the crystal fields as a perturbation, whose essential role is to established favored directions of the moments in the lattice. The "exotic" spin configurations may be understood as the result of a compromise between the above three competing interactions, to which the moments are subjected. Since the interactions are temperature-dependent, different interactions prevail in different temperature ranges, so that the magnetic structures change with the temperature. As a rule, the high-temperature magnetically ordered structure is AFM, which transforms to FM upon cooling (Gd is an exception, undergoing directly the paramagnetic to FM transition). In the FM state, the moments at low temperatures and in moderate magnetic fields approach their maximum saturation values of $g\mu_B J$, where g is the Landé factor, μ_B is the Bohr magneton and J is the total angular momentum quantum number.

Mixing of five or more heavy-RE elements into a HEA results in rich magnetic field-temperature phase diagrams. Random distribution of the elements on the crystal lattice results in distributions of atomic magnetic moments, exchange interactions, magnetocrystalline anisotropy and dipolar interactions. Beside the periodic potential experienced by the localized moments, which arises from the electronic band structure and favors periodic magnetic structures, chemical disorder introduces additional random local potential that favors spin-glass (SG)-type spin freezing in random crystal directions at low temperatures. In an external magnetic field, the Zeeman interaction favors spin alignment along the field direction. Due to the competition of these interactions, the heavy-RE-based HEAs GdTbDyHoLu [5], TbDyHoErTm [6] and GdTbDyHoY [3] were shown to undergo first a transition to an AFM structure, which upon cooling "melts" and transforms into a low-temperature SG-type collective spin state, either speromagnetic, asperomagnetic or a "true" spin glass. A high enough external magnetic field coerces all the moments into the field direction, creating a metamagnetic (field-induced) paramagnetic state. The addition of the light-RE Ce into the CeGdTbDyHo HEA [4] changes the situation drastically, where the alloy undergoes in zero field a single magnetic phase transition to a disordered FM state.

The light half of the lanthanide series (from Ce to Eu) is much less understood [15]. Pure light-RE metals crystallize predominantly in a double hexagonal close-packed (dhcp) structure, with the close-packed layers stacked along the *c* hexagonal direction in the sequence ABAC, as compared to ABAB of the hcp structure. The dhcp structure contains two types of crystallographic sites (Wyckoff sites 2*a* and 2*c*). For an ideal $c/2a = 1.633$ ratio, the A sites in 2*a* possess local cubic symmetry (3 *m*.) with nearest neighbors close to the fcc configuration, while the B and C sites in 2*c* possess local hexagonal symmetry (–6*m*2). If the $c/2a$ ratio is smaller from the ideal value, the cubic sites have only approximate local cubic symmetry. Since the CF interaction depends on the local site symmetry, the sites A possess different CF interaction than the B and C sites. This is in contrast to the hcp structure of the heavy RE metals, which contains only one type of a site (2*c*), having local hexagonal symmetry (–6*m*2) and consequently a single type CF interaction. Another important difference to the heavy REs is the balance between the exchange (a two-ion interaction) and the CF (a single-ion interaction), which in the light REs is not so clear-cut. The de Gennes factor G that scales the RKKY interaction is relatively smaller in the light RE, making the exchange weaker, while larger spatial extension of the 4 *f* orbitals towards the beginning of the lanthanide series (due to the known lanthanide contraction with increasing atomic number Z) makes the CF effects more important. Unlike the heavy RE metals, the CF interaction in the light RE cannot be considered just a perturbation to the exchange. As a result, the crystal fields in the light-RE metals are able to hinder the moments from attaining their saturation values of $g\mu_B J$ even in high fields at low temperatures. The magnetic structures of the light-RE metals are phenomenologically reasonably well described [15], while their theoretical explanations are still at a rudimentary stage. Magnetic ordering is strictly AFM, where the moments at the hexagonal sites of the dhcp structure order at a higher temperature than the cubic sites. Light-RE metals are also special from the magnetic excitations point of view, as they contain specific crystal-field excitations, sometimes called magnetic excitons. These represent collective normal modes of the spin system, associated with transitions between different energy levels of the CF ground-state multiplet with an overall splitting of the order 10–20 meV.

Due to the above-described differences between the heavy- and the light half of the lanthanides, it is tempting to design and determine the structural and physical properties of a HEA composed exclusively from the light lanthanides and compare it to the HEAs based on the heavy REs. In this paper, we present a study of the light-RE alloy series $Ce_xPrNdSm$ with the nominal Ce content in the range $x = 0.01$–1.5. To the best of our knowledge, the light-RE HEAs have not been reported in literature as yet to date.

2. Materials design and synthesis

By excluding the radioactive promethium (Pm), there are five magnetic light lanthanides: cerium (Ce), praseodymium (Pr), neodymium (Nd), samarium (Sm) and europium (Eu). In order to produce a single-phase HEA with random mixing of the elements on a topologically undistorted crystal lattice (a definition of an ideal HEA), it is advantageous to mix the elements with close-to-zero binary mixing enthalpies and very similar atomic radii. The binary mixing enthalpies ΔH^{ij}_{mix} of the elemental pairs i,j constituting a hypothetical five-component HEA Ce-Pr-Nd-Sm-Eu are presented in Table 1 [16], where it is evident that the elements Ce, Pr, Nd and Sm mix ideally ($\Delta H^{ij}_{mix} = 0$ for any pair), while Eu possesses quite substantial positive (repulsive) binary mixing enthalpies in the range 12–14 kJmol^{-1} with the other four elements. From this criterion, Eu will not mix well with the other four elements in the alloy, but will tend to segregate. Atomic radii of the elements are presented in Table 2 [16], where it is evident that Eu ($r_{Eu} = 0.199$ nm) is a significantly bigger atom than the other four, which are very close in size to each other (0.179–0.183 nm). Random mixing of the Eu into a 5-component HEA will hence be compromised also from this criterion. Accordingly, we decided to skip Eu and produce a 4-component alloy Ce-Pr-Nd-Sm that can be expected to form an ideal-like, single-phase random solid solution. Based on the mixing entropy criterion by Yeh [17], where the mixing entropy of an ideal solid solution with equiatomic concentrations of N components is written as $\Delta S_{mix} = R\ln N$ (with R denoting the gas constant), the alloys classify as HEAs for $\Delta S_{mix} > 1.5R$, which is achieved by mixing five or more elements ($N \geq 5$) [17–21]. The alloys composed of three or four elements possess $1R < \Delta S_{mix} < 1.5R$ and are classified as medium-entropy alloys (MEAs). The 4-component Ce-Pr-Nd-Sm alloys hence formally classify as MEAs. The room-temperature (RT) crystal structures of the light-lanthanide metals are presented in Table 2 [15], revealing that Ce has two stable RT modifications (dhcp and fcc), while Pr, Nd and Sm crystallize in the dhcp. Among the light RE, Ce is exceptional because being at the beginning of the lanthanide series (having one 4 *f* electron), the spatial extent of its 4 *f* wave function is the largest, so that the interaction with the surrounding charges in a crystal is the strongest. The Ce metal and compounds consequently constitute a field of magnetism in themselves.

Table 1
Binary mixing enthalpies (in kJmol^{-1}) for unlike atom pairs constituting a hypothetical Ce-Pr-Nd-Sm-Eu HEA [16].

Ce	0	0	0	12
0	Pr	0	0	13
0	0	Nd	0	13
0	0	0	Sm	14
12	13	13	14	Eu

Table 2
Atomic radii of the elements [16] and room-temperature crystal structures of the pure light-RE metals.

Element	Atomic radius (nm)	RT crystal structure
Ce	0.183	dhcp, fcc (two stable modifications)
Pr	0.183	dhcp
Nd	0.182	dhcp
Sm	0.179	dhcp
Eu	0.199	bcc

Their properties vary from highly localized magnetism, often with very anisotropic interactions, through mixed-valence systems with heavily quenched moments, to nonmagnetic heavy-fermion superconductors. Due to the unprecedented performance of Ce, we decided to vary its content in the alloys from diluted to the concentrated limit, by synthetizing a series of MEAs $Ce_xPrNdSm$, where the contents of Pr, Nd and Sm in each alloy were kept nominally equal, while the Ce content was varied in the range $x = 0.01$–1.5.

We have prepared five $Ce_xPrNdSm$ MEAs with the nominal Ce contents $x = 0.01$, 0.1, 0.2, 1.0 and 1.5 by arc-melting stoichiometric amounts of the constituent elements under an argon atmosphere. The total weights of the resulting polycrystalline ingots after arc melting were reduced by 3–10 % with respect to the initial weights, due to the elements' evaporation. The materials were investigated in an as-cast state. After cutting and polishing, the samples for measurements were kept in ethanol to reduce their oxidation and corrosion in the air atmosphere. In the following, we will use an abbreviated denotation of the samples according to their nominal Ce contents (e.g., the $Ce_{0.01}PrNdSm$ sample will be abbreviated as $x = 0.01$). The three alloys $x = 0.01$, 0.1 and 0.2 will be referred to as low-Ce content alloys, while the alloys $x = 1.0$ and 1.5 will be referred to as Ce-concentrated alloys.

3. Structural and chemical characterization

3.1. X-ray diffraction

Crystal structures were identified by powder X-ray diffraction (XRD) using monochromatic Cu $K\alpha_1$ radiation. The XRD patterns of all five alloys in the range of diffraction angles $10° < 2\theta < 100°$, with the Ce content x increasing from top to bottom, are shown in Fig. 1. All alloys are single-phase and crystallize in the dhcp structure, with negligible traces of other phases. The intensities of the reflections did not match the theoretical powder intensities, indicating some preferential orientation of the grains in the polycrystalline ingots. For that reason, the Le Bail fitting procedure (refining the unit cell based on the positions of the reflections and adjusting the intensities individually to fit best) was used to determine the unit cell parameters. An attempt to reproduce also the intensities was made by assuming a coexistence of two phases, a hcp and a dhcp, with the same a parameter, while the c parameters were in the ratio 1:2. In that case, a number of peaks are common to both phases, whereas some are dhcp-specific. For such model, it could happen that a certain combination of the hcp and dhcp phase fractions would reproduce well also the peak intensities. Performing fitting, no such combination could be found, supporting the consideration that the intensity mismatch originates from the dhcp-phase grains' preferential orientation. Bragg positions of the dhcp reflections, calculated for the unit cell parameters of the $x = 1.5$ alloy are shown by tick marks at the bottom of Fig. 1 (and also given in Table S1 of the Supplementary material).

The dhcp unit cell parameters are collected in Table 3 (and plotted as a function of the Ce concentration in Fig. S1 of the Supplementary material), showing that the a and c parameters both increase monotonously with increasing x (from $a = 3.6571$ Å, $c = 11.778$ Å in the $x = 0.01$ alloy to $a = 3.6690$ Å, $c = 11.810$ Å in $x = 1.5$, thus by about 0.3 % in the interval $x = 0.01$–1.5). This reflects the fact that the increased concentration of the large-radius element Ce in the alloys slightly expands the lattice. The $c/2a$ ratio ranges from 1.610 for $x = 0.01$ to 1.609 for $x = 1.5$ (Table 3), being smaller than the ideal value 1.633 for the entire $Ce_xPrNdSm$ series.

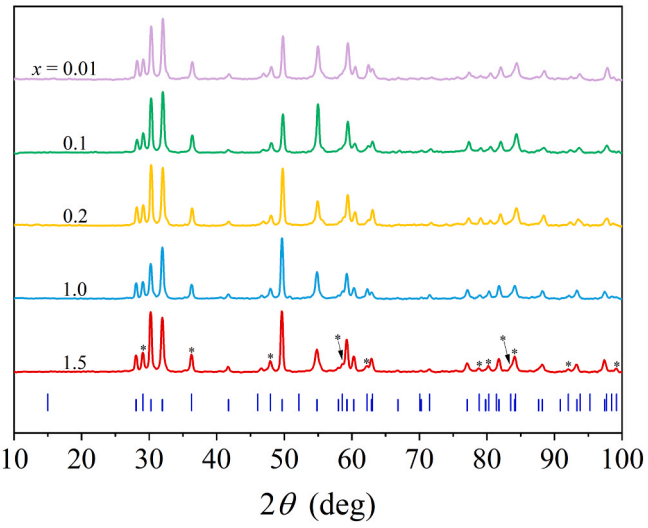

Fig. 1. XRD patterns of the $Ce_xPrNdSm$ ($x = 0.01$– 1.5) MEAs at room temperature, with the Ce content x increasing from top to bottom. Bragg positions of the dhcp-phase reflections, calculated for the unit cell parameters of the $x = 1.5$ alloy are shown by tick marks at the bottom (also given in Table S1 of the Supplementary material). The reflections that are common to the hcp and dhcp phases with the same a, but c in the ratio 1:2, are represented by shorter sticks, while the reflections appearing only in the dhcp, but absent in hcp, are represented by longer sticks. Some dhcp-specific reflections (those of a significant intensity) are marked by asterisks on the trace of the $x = 1.5$ alloy.

3.2. SEM imaging and EDS chemical analysis of the microstructure

Scanning Electron Microscopy (SEM) backscattered-electron (BSE) imaging and Energy Dispersive X-ray Spectroscopy (EDS) were used to investigate the microstructure and chemical composition of the alloys. The surfaces were first polished with a diamond paste and then prepared in vacuum by Focused Ion Beam (FIB) technique using gallium ions, to remove the oxidized and corroded surface layer of about 20–40 μm thickness (depending on the position). In the following we present the results for the $x = 0.2$ alloy, which is representative of all alloys. The SEM BSE image of the surface on the μm scale is presented in the upper left panel of Fig. 2, where it is observed that the light-grey matrix is homogeneous on this spatial scale, but contains one considerably darker elongated region. The EDS elemental maps of the elements Ce, Pr, Nd, Sm, and in addition the oxygen O, are shown in other panels of Fig. 2. The elemental maps identify the dark elongated region as the RE oxide, which was not completely removed by the FIB surface treatment (some oxidized regions may also be present in the bulk material, due to pre-oxidation of the pure elements used for the synthesis). Disregarding the oxide, the EDS elemental maps of the Ce, Pr, Nd and Sm elements reveal that their distribution is homogeneous, confirming that the $x = 0.2$ material is a single-phase random solid solution on the μm scale. A homogeneous distribution of the elements on the μm scale is further supported by the SEM-EDS elemental line profiles over the path of 10-μm length that crosses the oxidized region (Fig. 3). The SEM BSE images and EDS elemental maps of other alloys are presented in the Supplementary material (Figs. S2–S5) and are in accordance with the above results.

The experimental chemical compositions of all five alloys, determined by the EDS point analysis (an average over ten points within the surface area of about 100 μm^2), together with the nominal compositions are given in Table 3, showing that the EDS compositions are not far from

Table 3
List of the investigated $Ce_xPrNdSm$ alloys, their nominal and SEM-EDS chemical compositions, the dhcp unit cell parameters and the $c/2a$ ratio.

Alloy (abbreviated name)	Alloy (nominal composition)	Alloy (nominal composition at%)	SEM-EDS composition (at%)	Lattice parameters (dhcp) (Å)	$c/2a$
$x = 0.01$	$Ce_{0.01}PrNdSm$	$Ce_{0.4}Pr_{33.2}Nd_{33.2}Sm_{33.2}$	$Ce_{0.5}Pr_{34.5}Nd_{35.7}Sm_{29.3}$	$a = 3.6571(2)$, $c = 11.778(1)$	1.610
$x = 0.1$	$Ce_{0.1}PrNdSm$	$Ce_{3.1}Pr_{32.3}Nd_{32.3}Sm_{32.3}$	$Ce_{3.1}Pr_{30.9}Nd_{32.1}Sm_{33.9}$	$a = 3.6574(2)$, $c = 11.779(1)$	1.610
$x = 0.2$	$Ce_{0.2}PrNdSm$	$Ce_{6.4}Pr_{31.2}Nd_{31.2}Sm_{31.2}$	$Ce_{7.0}Pr_{31.5}Nd_{35.0}Sm_{26.5}$	$a = 3.6603(2)$, $c = 11.783(1)$	1.610
$x = 1.0$	$Ce_{1.0}PrNdSm$	$Ce_{25.0}Pr_{25.0}Nd_{25.0}Sm_{25.0}$	$Ce_{26.4}Pr_{26.9}Nd_{28.2}Sm_{18.5}$	$a = 3.6676(2)$, $c = 11.804(1)$	1.609
$x = 1.5$	$Ce_{1.5}PrNdSm$	$Ce_{33.4}Pr_{22.2}Nd_{22.2}Sm_{22.2}$	$Ce_{34.1}Pr_{23.0}Nd_{23.7}Sm_{19.2}$	$a = 3.6690(2)$, $c = 11.810(1)$	1.609

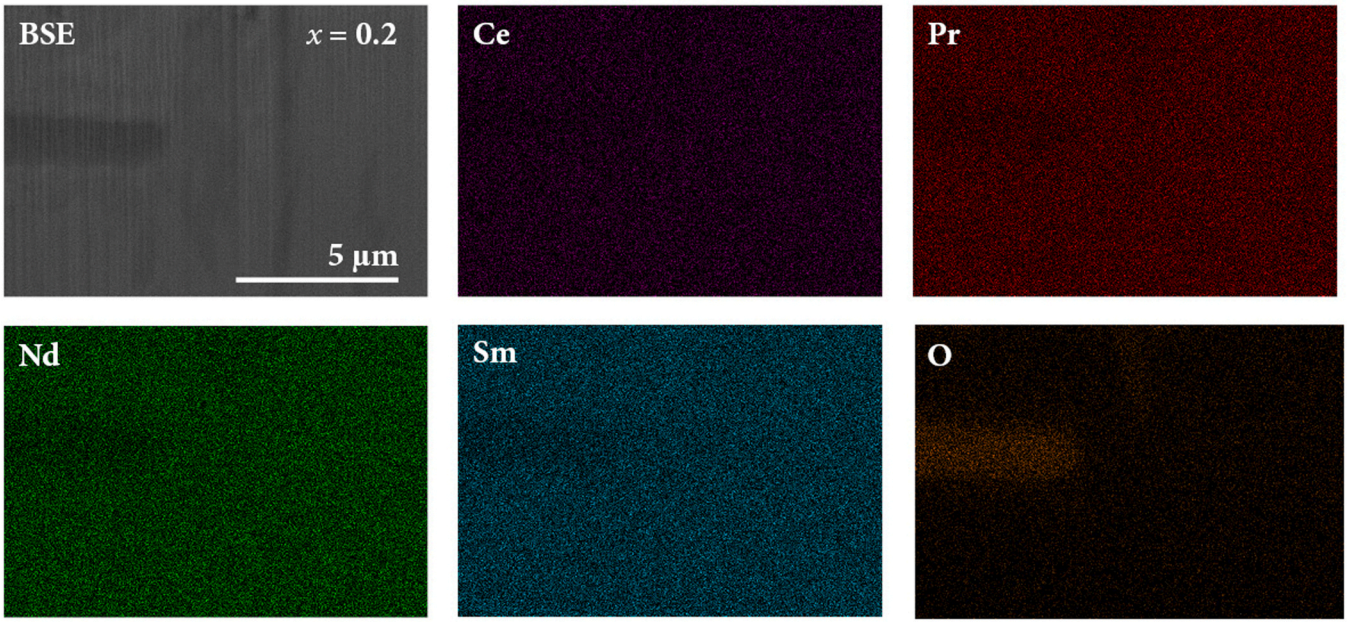

Fig. 2. SEM-BSE image (upper left panel) and SEM-EDS elemental maps of the $x = 0.2$ alloy. The oxygen map is shown as well.

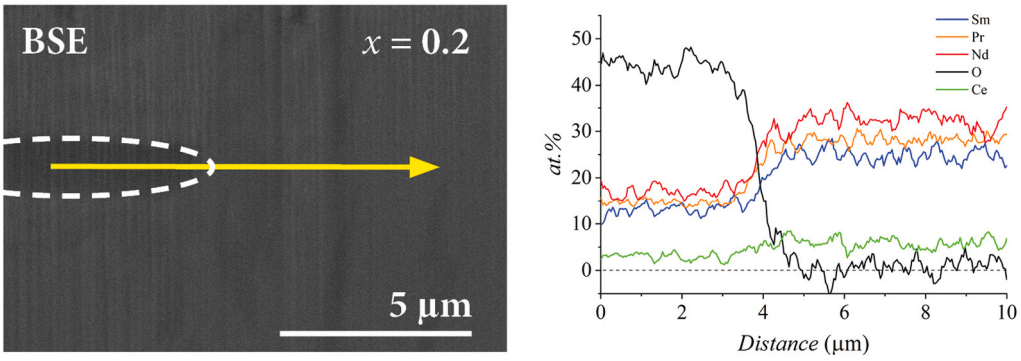

Fig. 3. SEM-EDS compositional line profiles of the elements in the $x = 0.2$ alloy (including oxygen), measured along a 10-µm path that crosses the oxidized region. The path is drawn in the BSE image (left panel), where the oxidized region is marked by the dashed oval.

the nominal ones.

3.3. TEM analysis of the nanostructure

The nanostructure was investigated by Transmission Electron Microscopy (TEM) methods of high-angle annular dark field (HAADF) and bright-field (BF) scanning TEM (STEM) imaging, STEM-EDS elemental mapping, electron energy loss spectroscopy (EELS) and selected area electron diffraction (SAED). The nanostructure was determined for two alloys of the $Ce_xPrNdSm$ series, the $x = 0.01$ (with the lowest Ce content) and $x = 1.5$ (with the highest Ce content). The lamellae of thickness about 100 nm for the TEM investigations were prepared by FIB using gallium ions.

The HAADF-STEM images of both alloys on two magnification scales are presented in Fig. 4, where it is evident that both show the nanostructure of numerous darker precipitates of about 50–100 nm cross dimension in a lighter matrix. Since the nanostructures of the two alloys are qualitatively similar, we analyze here the nanostructure of the $x = 1.5$ alloy and consider it representative of all investigated $Ce_xPrNdSm$ alloys, while the nanostructure of the $x = 0.01$ alloy is discussed in the Supplementary material (and detailed in Figs. S6 and S7). The HAADF contrast observed in Fig. 4 could be due to (1) compositional inhomogeneities (precipitates having lower average atomic number than the matrix), (2) structural differences (precipitates having different

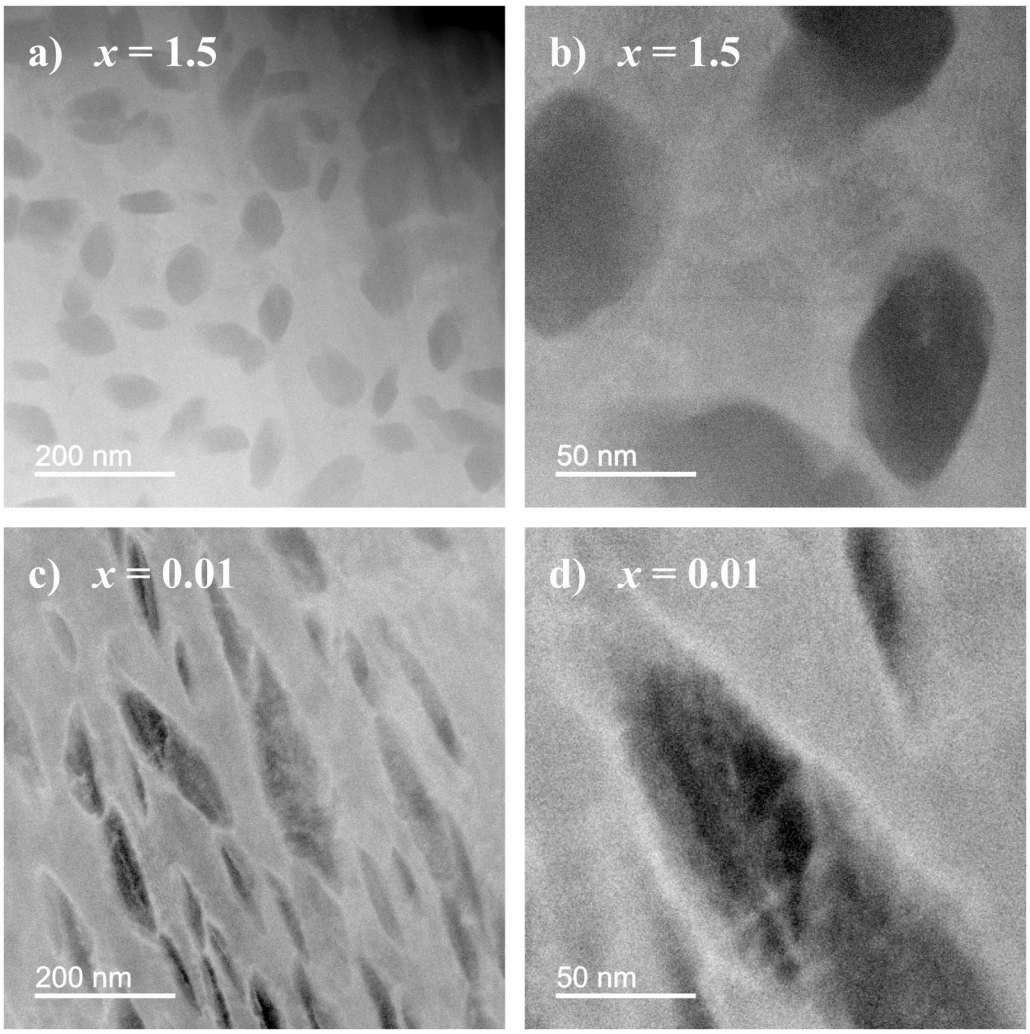

Fig. 4. HAADF-STEM images on two magnification scales of the $x = 1.5$ alloy (panels (a) and (b)) and the $x = 0.01$ alloy (panels (c) and (d)).

crystal structure than the matrix), (3) thickness difference (precipitates being thinner than the matrix) and (4) orientation difference (precipitates having the same crystal structure as the matrix, but are in a different crystallographic orientation). These four possibilities were systematically checked by EDS elemental mapping, EELS spectroscopy (thickness measurement) and diffraction (structure and orientation). The STEM-EDS elemental maps of the $x = 1.5$ alloy (Fig. 5a) do not show any significant differences between the matrix and the precipitates, revealing that the chemical composition of both is more or less identical (the STEM-EDS composition of both was about $Ce_{34}Pr_{23}Nd_{24}Sm_{19}$, matching excellently the SEM-EDS average composition $Ce_{34}Pr_{23}Nd_{24}Sm_{19}$), thus ruling out the compositional inhomogeneities as the origin of the HAADF contrast. The possibility of thickness difference was checked by EELS at several locations marked by numbers 1–6 in the BF-STEM image (Fig. 5b) that include both the matrix and the precipitates (recall that the contrast of the BF image is inverted with respect to the HAADF image, so that the precipitates in BF appear bright). The results are presented in Fig. 5b (the estimated error is around 10 %), demonstrating the absence of any significant deviations in thickness over the studied plate.

The possible structural and orientational differences between the precipitates and the matrix were studied by electron diffraction. The SAED pattern of the $x = 1.5$ alloy is shown in Fig. 6a. At first glance, the diffraction spots (actually groups of spots) look like they represent the [001] zone of a hexagonal structure, but the spots are surprisingly not single, but rather complex groups of spots, where the complexity is better visible on the spots with larger Miller indices (the spots far from the center). The zoomed central part of the SAED pattern is shown in Fig. 6b. The powder XRD results (paragraph *3.1.*) have revealed that the material is a single-phase dhcp solid solution with the unit cell parameters $a \approx 3.67$ Å and $c \approx 11.8$ Å. If the zone of the diffraction pattern in Fig. 6 were [001], the six spots closest to the center would have the Miller indices *hkl* of the 100 family (100, 010, $\bar{1}10$, $\bar{1}00$, $0\bar{1}0$ and $1\bar{1}0$) and would all have the same interplanar spacing *d* value of 3.18 Å. The *d* values measured in the SAED pattern (Fig. 6b) show that this is not the case. Just one Friedel pair has the expected value of 3.19 Å (the difference of 0.01 Å between the XRD and SAED is insignificant as the SAED is not very precise; the match is in fact very good). The corresponding peak in the XRD pattern (the $x = 1.5$ trace of Fig. 1) is at about 28.1° 2θ. The other two Friedel pairs have the *d* values, calculated from the SAED, of 3.07 Å and 3.08 Å. This is in a very close agreement with the unit cell derived from XRD, where the reflections of the 101 family have the *d* value of 3.07 Å and the corresponding XRD peak is at about 29.0°. This means that the zone axis (or one of the zone axes) of the grains that are irradiated by the broad parallel beam in the SAED experiment (the diameter of the SAED circular aperture was 1 μm) must be such that some reflections from the 100 and 101 families are observed simultaneously. Such zones are of the type [101] and [111] (uvw notation). The small difference (in terms of the SAED resolution) between the two measured *d* values (3.19 and 3.07 Å) arises from the c/a ratio of the dhcp structure of the studied alloy. The assumption that the two *d* values belong to two dhcp structures in similar orientation, but differing in the

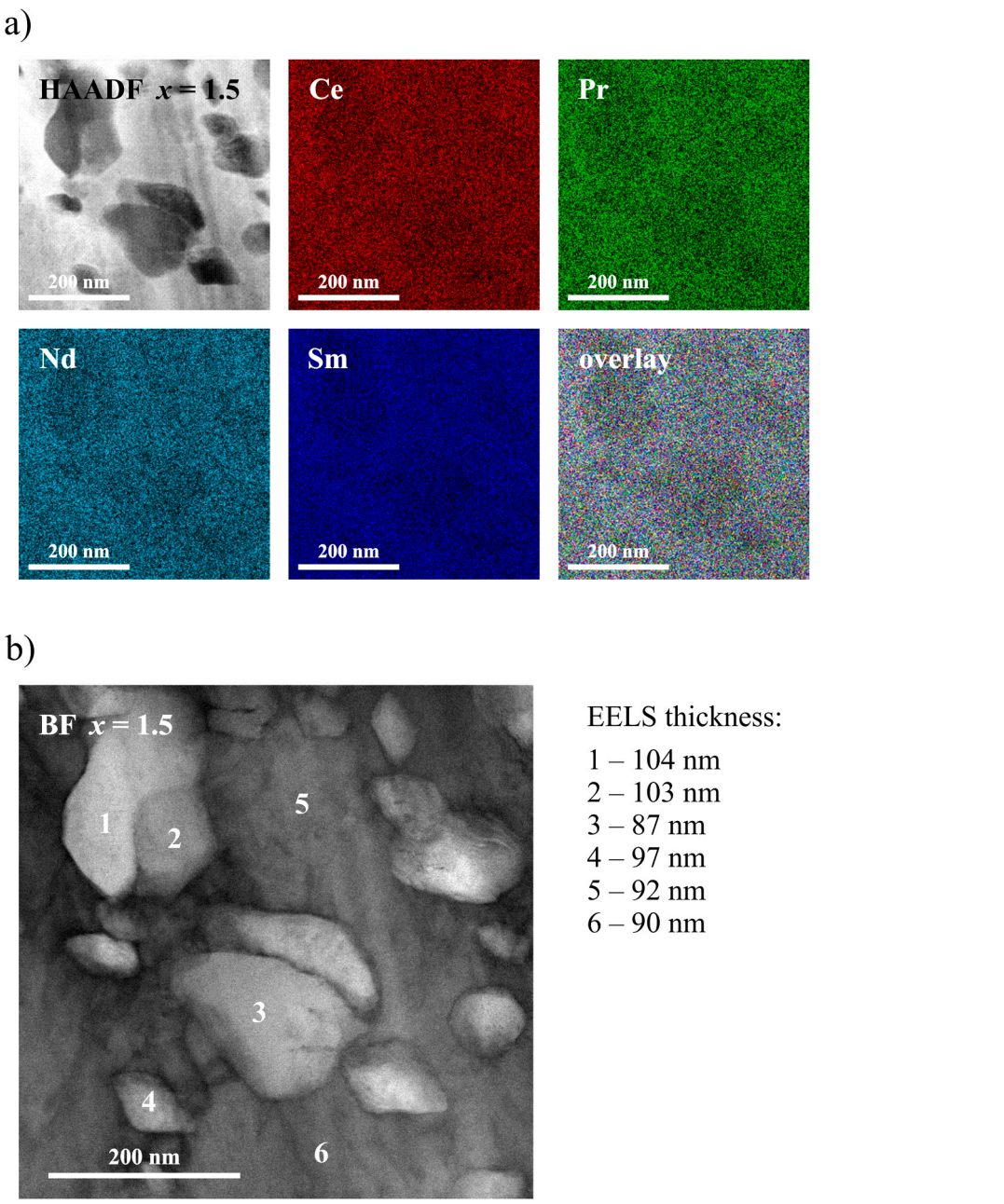

Fig. 5. (a) STEM-EDS elemental maps of the $x = 1.5$ alloy. The HAADF-STEM image of the investigated area is shown in the upper left panel. (b) BF-STEM image of the same area, where the numbers denote the locations of the EELS thickness determination. The thickness values are also given (the estimated error is around 10 %).

unit cell parameters is not realistic – the two unit cells would differ so much that this would be clearly seen in the XRD powder pattern (the peaks of the two structures would be separated for about a degree).

The multiple spots that become increasingly more visible at larger diffraction angles (smaller d values, larger Miller indices) can be explained by a superposition of diffraction patterns of multiple grains having the same crystal structure but different orientation around a common zone axis. We illustrate this presumption by an idealized model of superposition of three simulated diffraction patterns of the dhcp structure with $a = 3.67$ Å and $c = 11.8$ Å. The zone axis was [111] (uvw) in all cases, but the second pattern is rotated by 120° and the third by 240° clockwise against the first one. The result is shown in Fig. 7, where empty circles/squares mark kinematically extinct reflections. Miller indices of some groups of reflections are also written. The simulation provides triplets of spots in each group that are increasingly more separated at larger diffraction angles.

The triplets of spots resulting from the above idealized model are obviously not enough to explain the experimental SAED pattern of Fig. 6, where many more spots are visible in the groups at higher angles. This means that there must be more grains in the beam, where their zone axes do not coincide perfectly with each other and also the mutual rotations are likely not exactly 120° and 240°, but deviate for a small amount from these values. This gives rise to several separated diffraction spots. Very similar simulation can be done with the zone axis [101]. In both cases there are some spots, which are observed in the experimental SAED pattern, but are not predicted in the simulations, based on kinematic approximation due to symmetry induced systematic extinctions. It can be speculated that the reason for observing these reflections can either be multiple diffraction (dynamic effect) or the presence of grains that are oriented along the [001] zone.

After all other reasons for observing the dark precipitates in the HAADF image have been ruled out, the above explanation confirms that

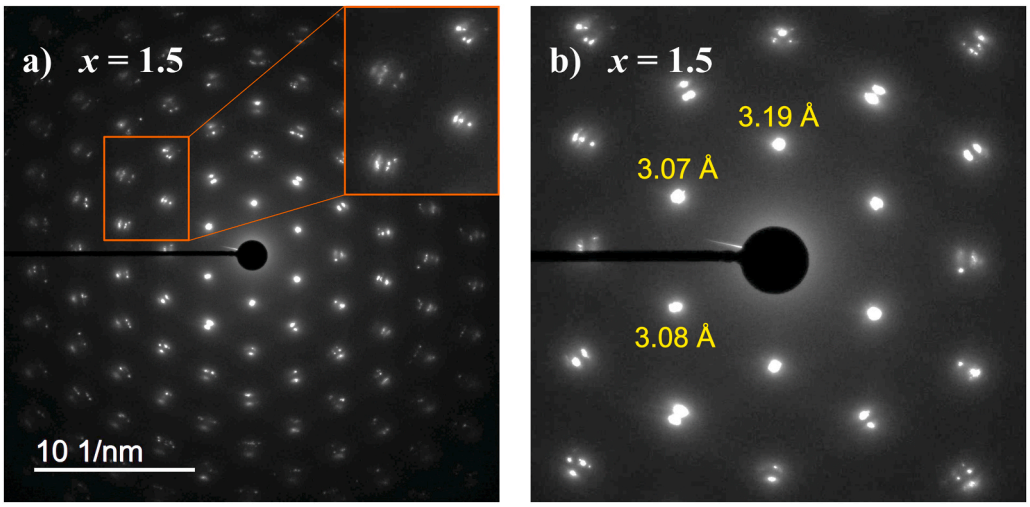

Fig. 6. (a) SAED pattern of the $x = 1.5$ alloy. The groups of reflections in the highlighted rectangle are shown magnified in the upper right corner of the panel. (b) Magnified central part of the SAED pattern. The interplanar spacings d of some reflections are also written.

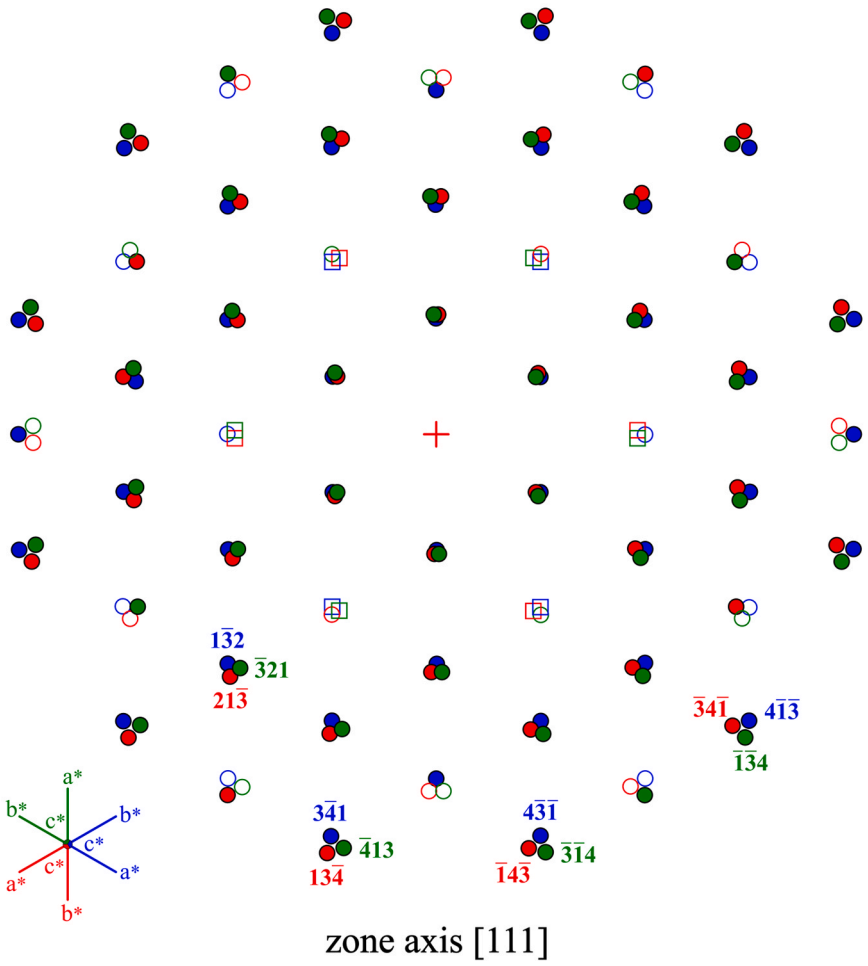

Fig. 7. Simulated SAED pattern of the $x = 1.5$ alloy (dhcp structure with $a = 3.67$ Å and $c = 11.8$ Å). The pattern is a superposition of three patterns, where the zone axis is [111] (uvw notation) in all cases. The second pattern (red) is rotated by 120° and the third (green) by 240° clockwise against the first one (blue). Empty circles/squares denote kinematically extinct reflections. Miller indices of some groups of reflections are also written.

the reason for the image contrast is the crystallographic orientation of the precipitates, which is different from the orientation of the matrix, but not random. The precipitates adopt various equivalent orientations that allow them to retain structural coherence with the matrix. It is possible that the underlying crystallographic process is twinning, but proving/disproving this hypothesis is beyond the scope of this work. Different orientation of the precipitates (grains) and varying electron channeling can also explain the tiny decrease in the intensity of all

elements in the STEM-EDS elemental maps presented in Fig. 5a.

4. Results

4.1. Direct-current magnetic susceptibility

Direct-current (dc) magnetic susceptibility $\chi = M/H$ was measured in the temperature interval from RT to 1.8 K in magnetic fields between $\mu_0 H = 0.5$ mT (equivalent to 5 G, in cgs units) and 7 T. The ultra-low-field option of the employed SQUID magnetometer was used to assure accurate and repeatable magnetic field setting in the low-field limit. The susceptibility was determined for both zero-field-cooled (zfc) and field-cooled (fc) protocols. The zfc and fc susceptibilities, χ_{zfc} and χ_{fc}, of all alloys in the lowest investigated field of 0.5 mT are shown in Fig. 8, where the following features are observed. χ_{zfc}s of the three low-Ce content alloys $x = 0.01$, 0.1 and 0.2 reveal a two-component structure, a $1/T$ Curie-type paramagnetic component and a relatively narrow peak, which appears at a temperature that decreases with the increasing Ce content x (i.e., the peaks in the $x = 0.01$, 0.1 and 0.2 alloys are located at temperatures 28, 26 and 22 K, respectively). The peak height increases slightly with x. The paramagnetic component is marked by an arrow in the χ_{zfc} of the $x = 0.1$ alloy. The fact that at the lowest temperatures (below about 5 K) the $1/T$-type growth of the paramagnetic component disappears and χ_{zfc} levels off can be attributed to increased interactions between the paramagnetic moments. χ_{fc}s, on the other hand, exhibit stronger growth in the same temperature range and the peak is broader, while the χ_{fc} values also increase slightly with x. The above behavior of χ_{zfc} and χ_{fc} is indicative of an inhomogeneous magnetic structure, consisting of paramagnetic domains of weakly coupled spins and domains of stronger coupled spins (spin clusters). The existence of the $\chi_{zfc} - \chi_{fc}$ difference indicates magnetic frustration and broken ergodicity on the experimental time scale of the clusters at low temperatures, bearing similarity to SGs. The two Ce-concentrated alloys $x = 1.0$ and 1.5 possess much larger χ_{zfc} and χ_{fc} susceptibilities (the χ_{fc} value of the $x = 1.5$ alloy at 2 K is larger by a factor of about 70 relative the $x = 0.01$ alloy), signaling strong increase of the magnetization of spin clusters. The χ_{zfc} and χ_{fc} of the $x = 1.5$ alloy are also significantly larger from those of the $x = 1.0$ alloy. The peaks in χ_{zfc} of these two alloys have further shifted down to lower temperatures relative to the three low-Ce content alloys, to about 11 K for both alloys. The zfc susceptibilities of all five alloys at temperatures below 40 K are plotted on the same graph in the lower right panel of Fig. 8, accenting the large increase of χ_{zfc} in the two Ce-concentrated alloys.

The fc susceptibility of the three low-Ce content alloys shows additional, FM-like component below about 100 K, marked in Fig. 8 by a dashed arrow in the panel of the $x = 0.2$ alloy. This FM component is present also in the χ_{fc}s of the two Ce-concentrated alloys, but cannot be observed in the respective graphs of Fig. 8 due to a much larger vertical scale. It is straightforward to associate this weak FM component with the RE oxides that are present in all investigated alloys (see Figs. 2 and 3, as well as Figs. S2–S5). It is known from literature that cerium(IV) oxide CeO_2, which is diamagnetic in its bulk crystalline fluorite form due to the Ce^{4+} valence state, exhibits weak ferromagnetism below RT when prepared in a nanopowder form or as nanoporous thin films [22,23]. The FM behavior has been ascribed to localized electron spin moments formed at oxygen vacancies near the nanosurfaces, estimating that a tiny volume part of about 0.1–0.5 % of the CeO_2 samples are ferromagnetic. While our SEM-EDS analysis cannot unravel which RE element in the $Ce_xPrNdSm$ MEAs forms the oxide (perhaps all four of them, either in the trivalent RE_2O_3 or tetravalent REO_2 forms), it is plausible that CeO_2 is present to some extent, being the origin (or one of the origins) of the tiny FM component in the fc magnetization. The oxides are, however,

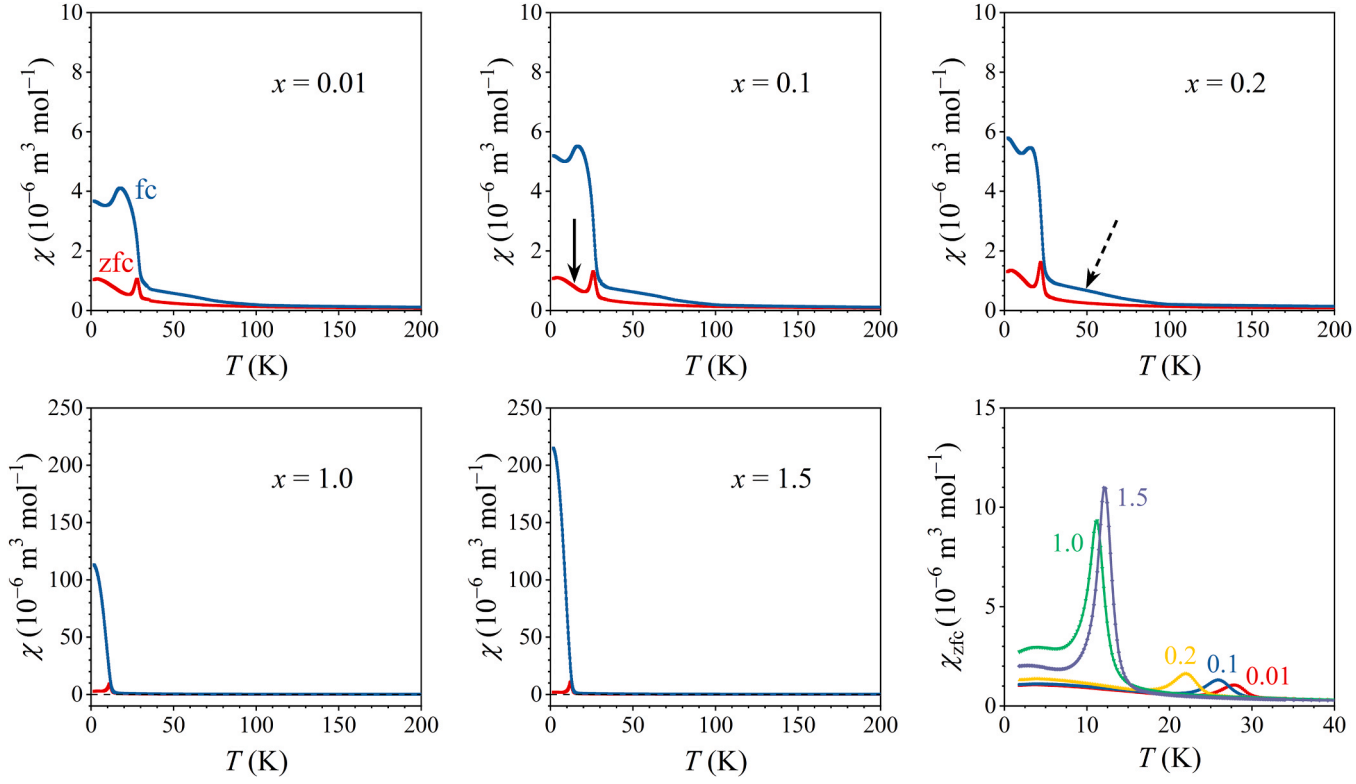

Fig. 8. Temperature-dependent zfc and fc dc susceptibilities, χ_{zfc} and χ_{fc}, of all alloys in the lowest investigated field of 0.5 mT (note the large change of the vertical scale on the graphs of the two Ce-concentrated alloys $x = 1.0$ and 1.5 relative to the three low-Ce content alloys). Solid arrow on the χ_{zfc} curve of the $x = 0.1$ alloy marks the paramagnetic component, while the dashed arrow on the χ_{fc} of the $x = 0.2$ alloy marks the FM component due to the CeO_2 oxide (see text). The zfc susceptibilities of all alloys on an expanded temperature scale below 40 K are plotted on the same graph in the lower right panel.

electrically insulating and do not contribute significantly to the magnetic phenomena in the metallic $Ce_xPrNdSm$ MEAs, because the RKKY interaction between the RE ions (which is mediated by the conduction electrons) is absent in the insulator.

The strength of the interaction responsible for the formation of the SG-like spin clusters (considered to be the RKKY indirect exchange) was investigated by performing measurements of χ_{zfc} and χ_{fc} in different magnetic fields up to 7 T and observing how the Zeeman interaction gradually destroys the internal magnetic structure by shifting the $\chi_{zfc} - \chi_{fc}$ bifurcation temperature towards lower temperatures and finally completely removing it (i.e., the $\chi_{zfc} - \chi_{fc}$ difference disappears). This is shown in Fig. 9 for two representative samples $x = 0.1$ and $x = 1.5$. For the $x = 0.1$ alloy, the $\chi_{zfc} - \chi_{fc}$ bifurcation at 1.8 K is still observed in a 5 T field, but is absent in 7 T, while for the $x = 1.5$ alloy, the bifurcation remains to be observed in a field of 2 T, but not higher. These values indicate that the internal magnetic structure is quite stiff, with the exchange interaction being a bit weaker in the $x = 1.5$ alloy, as compared to the $x = 0.1$. One of the effects of increased cerium content in the $Ce_xPrNdSm$ MEAs is hence slight weakening of the exchange interaction.

4.2. Paramagnetic susceptibility

At temperatures above the $\chi_{zfc} - \chi_{fc}$ bifurcation temperature, the susceptibility of all alloys becomes magnetic field-independent up to the highest field of 7 T, indicating the paramagnetic regime. The paramagnetic susceptibility was analyzed by the expression

$$\chi = C/(T-\theta) + \chi_0, \quad (1)$$

where the first term represents the Curie-Weiss susceptibility of localized paramagnetic moments, with C denoting the Curie-Weiss constant and θ the Curie-Weiss temperature, while the term χ_0 is the temperature-independent part of the susceptibility (a sum of the negative diamagnetic atomic core susceptibility χ_{Larmor}, the positive paramagnetic Pauli spin susceptibility χ_{Pauli} of the conduction electrons and the negative diamagnetic Landau susceptibility χ_{Landau} due to the conduction-electron orbital circulation in a magnetic field, where in the independent-electron approximation, the absolute values of all three contributions are of the same order of magnitude). The susceptibility of all alloys in the field of 3 T is shown in Fig. 10 in a $(\chi - \chi_0)^{-1}$ versus T plot, in a separate panel for each alloy. The fits with Eq. (1) of the high-temperature data between RT and 75 K are presented by solid lines and the fit parameter values are collected in Table S2 of the Supplementary material. The mean effective paramagnetic Bohr magneton number $\overline{p}_{eff}$ that determines the mean effective paramagnetic moment $\overline{\mu}_{eff} = \overline{p}_{eff}\mu_B$ per average atom of the alloy (e.g., per one $Ce_{0.031}Pr_{0.309}Nd_{0.321}Sm_{0.339}$ "atom" in the case of the $x = 0.1$ alloy) was extracted from the Curie-Weiss constant, using the relation $\overline{p}_{eff} = \left(797.7\sqrt{\mathrm{mol/m^3K}}\right)\sqrt{C}$ [24]. The results are presented in the lower right panel of Fig. 10, where it is observed that the $\overline{p}_{eff}$ values of all alloys are very much the same (not depending significantly on the Ce content x), being scattered randomly around the value 2.86. This result seems surprising at first glance, but becomes understandable when comparing the experimental $\overline{p}_{eff}$ values of the alloys to their composition-averaged theoretical (calculated) values $\overline{p}_{calc} = \left(\sum_{i=1}^{4} c_i g_i^2 J_i(J_i+1)\right)^{1/2}$, where i = Ce, Pr, Nd, Sm, c_i is the EDS concentration of the i-th element in the alloy, while the g_i and J_i values of the employed RE ions are collected in Table 4. For example, the composition-averaged theoretical Bohr magneton number of the $x = 0.01$ alloy with the EDS composition $Ce_{0.5}Pr_{34.5}Nd_{35.7}Sm_{29.3}$ amounts to $\overline{p}_{calc} = 3.05$, as compared to the $\overline{p}_{eff} = 2.80$ experimental value. The theoretical Bohr magneton numbers of all alloys are also presented in the lower right panel of Fig. 10, being close to their respective experimental values and do not depend significantly on the Ce content x. This elucidates the apparent independence of the experimental paramagnetic $\overline{\mu}_{eff}$ on x.

The Curie-Weiss temperatures of all alloys are negative, with the values in the interval $\theta \approx -4$ to -8 K and estimated uncertainty of ± 2 K. The dominant spin coupling in the $Ce_xPrNdSm$ MEAs is hence AFM (antiparallel) type, which is consistent with the fact that pure metals of the employed RE elements all order AFM at low temperatures (their Néel temperatures T_N are given in Table 4). As the experimental uncertainty is of the same order as the θ values themselves, no systematic variation of θ with the Ce content x can be claimed. The experimental χ_0 values of all alloys were found slightly positive, in the range $[6.1–7.5] \times 10^{-9}$ m^3mol^{-1}, indicating dominance of the Pauli paramagnetic spin susceptibility. Comparison to the Larmor diamagnetic susceptibility calculated from literature tables [25], which for e.g. the $x = 0.1$ alloy amounts to $\chi_{Larmor} = -2.5 \times 10^{-10}$ m^3mol^{-1} confirms the expected order of magnitude of χ_0.

4.3. Alternating-current magnetic susceptibility

Alternating-current (ac) magnetic susceptibility was determined in a sinusoidal magnetic field of amplitude $\mu_0 H_0 = 0.2$ mT at nine frequencies ν in the range 0.316–1000 Hz. The real part of the ac susceptibility χ' of all alloys in the low-temperature range (where the $\chi_{zfc} - \chi_{fc}$ splitting in the dc susceptibility starts to be observed) is presented in Fig. 11. In all cases, a frequency-dependent peak in χ' is observed at a temperature that coincides with the peak in the dc χ_{zfc}. This can be

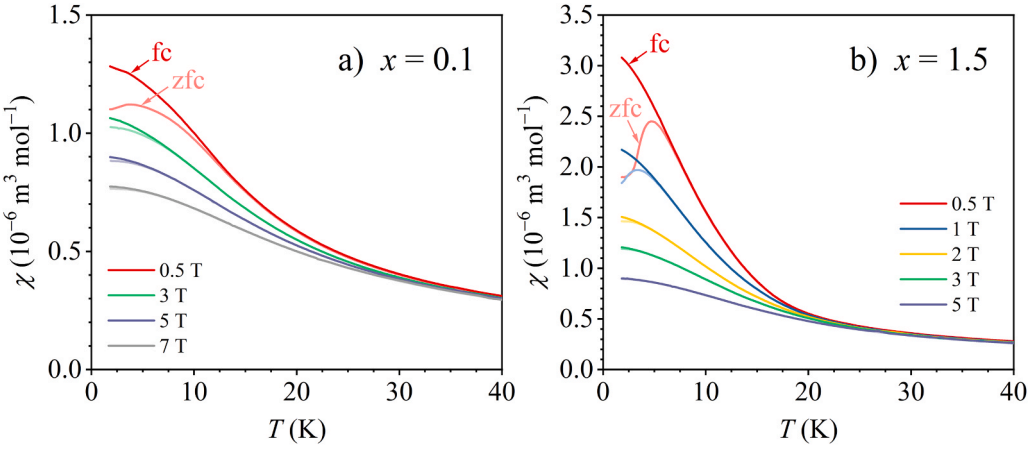

Fig. 9. Magnetic-field dependence of χ_{zfc} and χ_{fc} at temperatures below 40 K in the fields up to 7 T for (a) $x = 0.1$ alloy and (b) for $x = 1.5$, demonstrating how the $\chi_{zfc} - \chi_{fc}$ bifurcation temperature shifts to lower temperatures with the field as the Zeeman interaction gradually destroys the internal magnetic structure.

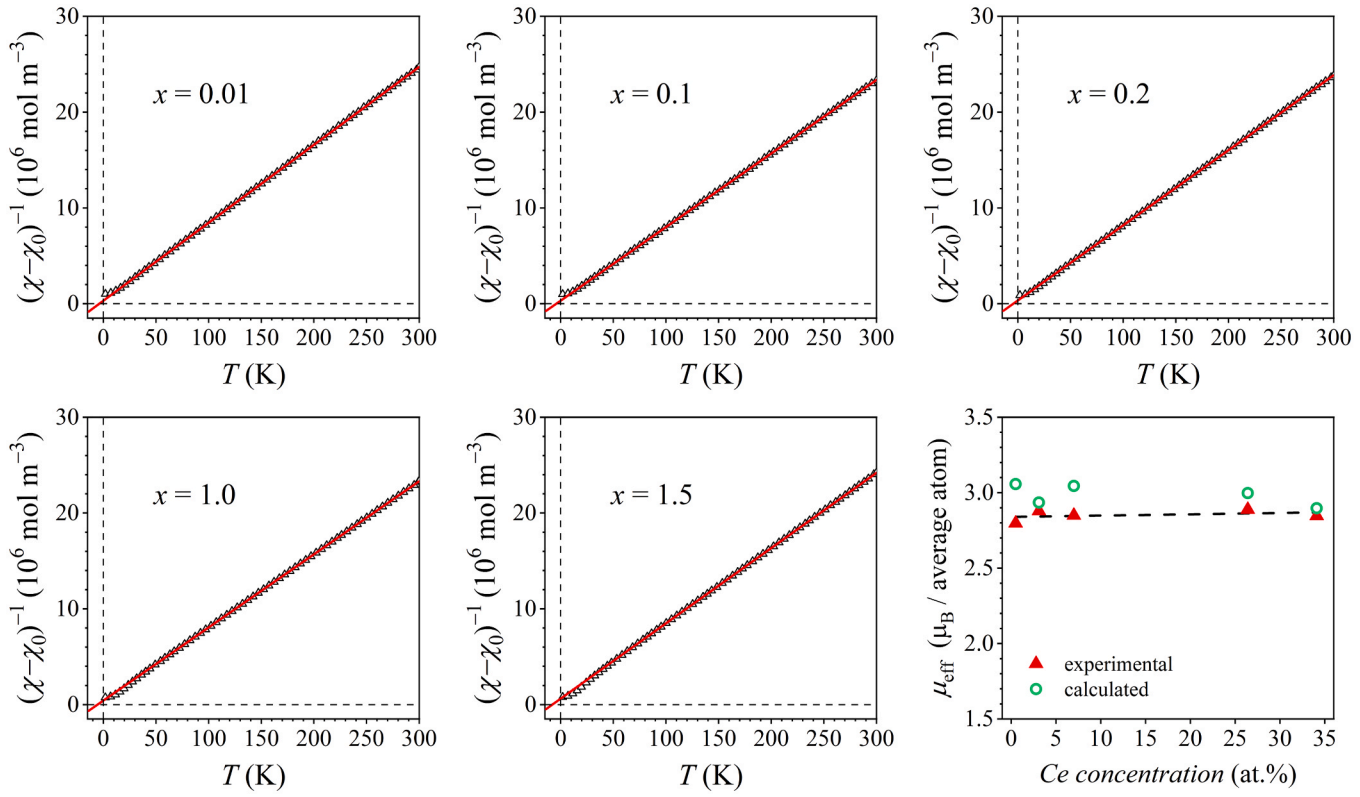

Fig. 10. Magnetic susceptibility of all alloys between RT and 1.8 K in the field of 3 T, presented in a $(\chi - \chi_0)^{-1}$ versus T plot. Solid lines are fits with Eq. (1) of the high-temperature data between RT and 75 K (for details see text). The lower right panel shows the experimental mean effective Bohr magneton number $\bar{p}_{eff}$ and the respective composition-averaged theoretical (calculated) $\bar{p}_{calc}$ value for each alloy, as a function of the Ce EDS concentration. The Bohr magneton numbers are presented per average atom of the alloy, e.g., per one $Ce_{0.031}Pr_{0.309}Nd_{0.321}Sm_{0.339}$ "atom" in the case of the $x = 0.1$ alloy. The horizontal dashed line at the value 2.86 represents the average of the experimental $\bar{p}_{eff}$s.

Table 4
Landé g-factor, total angular momentum quantum number J, de Gennes factor $G = (g-1)^2 J(J+1)$ of triply ionized ions and Néel temperatures T_N of the magnetic moments at the hexagonal and cubic sites of the dhcp pure metals [15].

Element	g	J	G	T_N (K)	
				hex.	cubic
Ce	6/7	5/2	0.18	13.7	12.5
Pr	4/5	4	0.80	0.05	
Nd	8/11	9/2	1.84	19.9	8.2
Sm	2/7	5/2	4.46	106	14.0

verified by comparing the $\chi'(0.316\ \text{Hz})$ susceptibilities of all alloys presented on the same graph in the lower right panel of Fig. 11 to the dc zfc susceptibilities χ_{zfc} presented in the lower right panel of Fig. 8, where good matching is observed. Upon increasing the frequency ν, the peak in χ' of each alloy shifts to higher temperatures and its amplitude diminishes. This is a fingerprint of broken ergodicity of the spin system on the experimental time scale, where the magnetically frustrated system contains a distribution of local magnetic moments of coupled spin entities. At low frequencies, most of the moments are able to follow the ac magnetic field instantaneously, whereas at elevated frequencies, large moments can no longer follow the field, while smaller moments still can, which results in the χ' amplitude decrease. In analogy to SGs, we associate the temperature of the peak in $\chi'(\nu)$ with the frequency-dependent spin freezing temperature $T_f(\nu)$. In Fig. 12, the relation $T_f(\nu)/T_f(0.316\ \text{Hz})$ is shown on a logarithmic frequency scale for all alloys, whereas the fractional shift of the spin freezing temperature per decade of frequency $\Gamma = \Delta T_f / T_f \Delta(\log\nu)$, as a function of the Ce content x is shown in the lower right panel of Fig. 12.

The ac susceptibility results show the following trends. (1) The magnitude of the χ' peak increases with x, where for the lowest frequency of 0.316 Hz, the maximum χ' value of the $x = 1.5$ alloy is by a factor 13 larger as compared to the $x = 0.01$ alloy, indicating an increase of the clusters' magnetization that contribute to the ac susceptibility signal. (2) For each alloy, the increasing frequency strongly diminishes the χ' amplitude, which almost vanishes at the highest frequency of 1000 Hz. This rapid decrease happens over a relatively narrow frequency interval, spanning over four orders of magnitude. (3) The spin freezing temperature T_f at a given frequency decreases with the increasing Ce content x in the alloys (note that the T_fs of the two Ce-concentrated alloys $x = 1.0$ and 1.5 are more or less equal). At the frequency of 0.316 Hz, the T_f of the $x = 0.01$ alloy amounts to 28.4 K, but shifts to about 12 K for the $x = 1.0$ and 1.5 alloys. (4) In contrast, the relative shift $T_f(\nu)/T_f(0.316\ \text{Hz})$ increases with the increasing Ce content x. While for the $x = 0.01$ alloy, the total relative shift in the frequency range 0.316–1000 Hz is by 2 %, the shift amounts to 7 % for the $x = 1.5$ alloy. (5) The associated fractional shift of the spin freezing temperature per decade of frequency Γ also increases with x. For the $x = 0.01$ alloy, $\Gamma = 6.6 \times 10^{-3}$, while it has increased to $\Gamma = 2.0 \times 10^{-2}$ for the $x = 1.0$ and 1.5 alloys. The Γ values in the range 10^{-3}–10^{-2} are typical for SGs (magnetically frustrated systems of coupled spins or spin clusters) [26]. For comparison, superparamagnets (systems of spin clusters that are uncoupled to each other) exhibit larger values of the order $\Gamma \approx 10^{-1}$. The above results confirm that the increased Ce content x increases the clusters' magnetization, but also weakens the interspin interactions in the $Ce_xPrNdSm$ MEAs, so that the clusters' moments become less coupled and more easily reorientable by the ac magnetic field (i.e., the moments' dynamics is gradually changing from SG-type

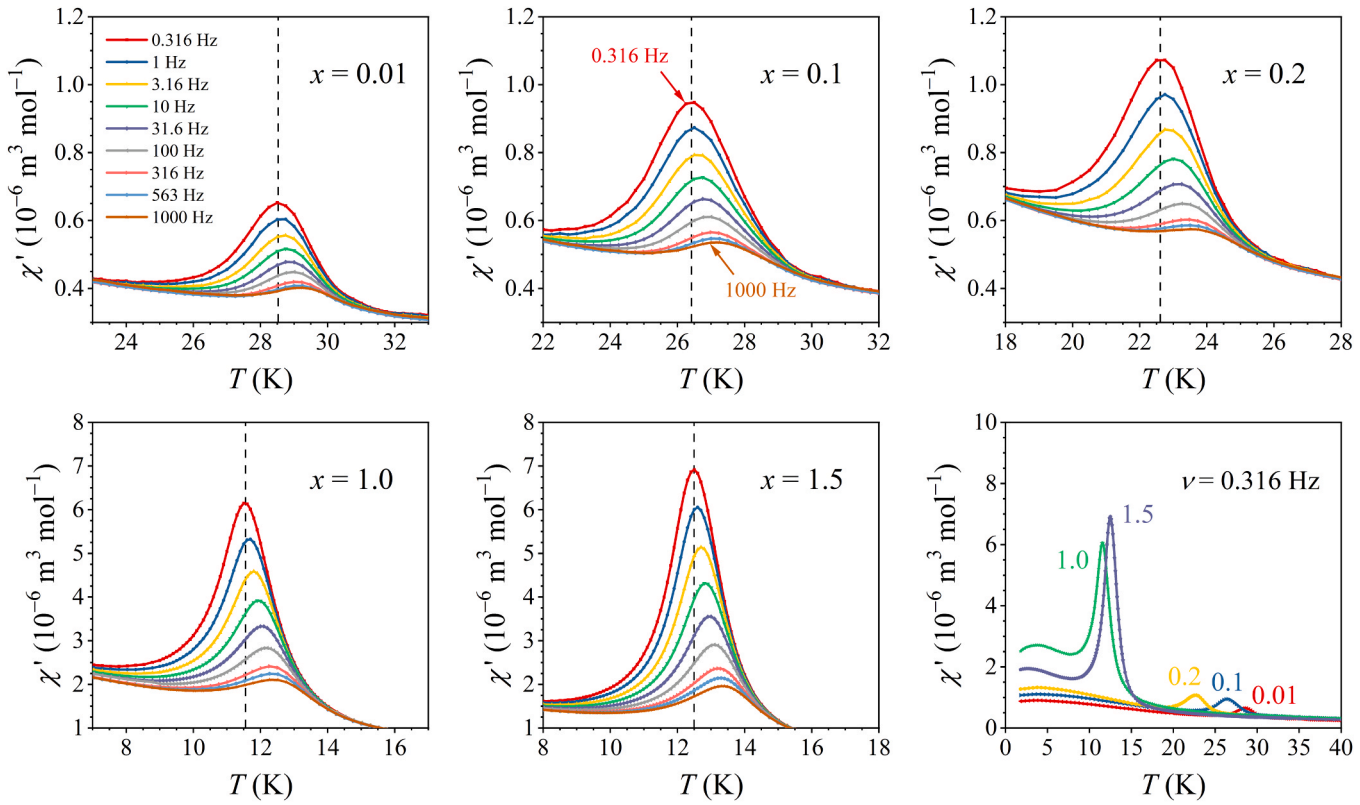

Fig. 11. Real part of the ac susceptibility χ' of all alloys in the low-temperature range, where the $\chi_{zfc} - \chi_{fc}$ splitting in the dc susceptibility starts to be observed. The width of the displayed temperature interval is the same on all graphs, while there is a change of the vertical scale for the two Ce-concentrated alloys relative to the three low-Ce content alloys. Vertical dashed line in each panel indicates the temperature of the χ' maximum at the lowest frequency of 0.316 Hz, associated with the spin freezing temperature T_f(0.316 Hz). The lower right panel shows χ' at the lowest frequency of 0.316 Hz of all alloys on an expanded temperature scale below 40 K.

into the direction of superparamagnets, though the superparamagnetic limit is not reached).

4.4. The $M(H)$ magnetization curves

The $M(H)$ magnetization versus the magnetic field curves were measured in a magnetic field sweep $\mu_0 H = \pm 7$ T at several temperatures between RT and 1.8 K. The curves of all alloys at the lowest temperature of $T = 1.8$ K are shown in Fig. 13, for each alloy in a separate panel. The three low-Ce content alloys $x = 0.01$, 0.1 and 0.2 exhibit narrow hysteresis, demonstrated on an expanded scale in the insets. The hysteresis loops of the $x = 0.01$ and 0.1 alloys close up in a field of about 3 T, while the loop of the $x = 0.2$ alloy closes in a bit lower field of about 2.5 T. Such close-up field values reveal predominant AFM-type hysteresis (FM-type hysteresis loops typically close in about 10-times lower fields). The hysteresis loops of the two Ce-concentrated alloys $x = 1.0$ and 1.5 are broader and the loops close up in a still lower field of about 2 T. The coercive field at 1.8 K of all alloys is presented in the lower right panel of Fig. 13, where it is seen that it increases linearly with the increasing Ce content x, ranging from $\mu_0 H_c \approx 37$ mT for the $x = 0.01$ alloy to $\mu_0 H_c \approx 253$ mT for $x = 1.5$. The $M(H)$ curves at $T = 10$ K, where the hysteresis is smaller, are shown in Fig. 14. Comparing the $M(H)$ curves of different alloys, we observe that the curves of the two Ce-concentrated alloys show qualitative difference to those of the three low-Ce content alloys. Namely, the former contain an additional magnetization component which increases with the field very rapidly in the low-field region, as demonstrated in the insets where the curves are shown on an expanded scale.

The $M(H)$ curves were analyzed theoretically. The fitting model for the three low-Ce content alloys was constructed following two experimental findings: (1) the dc susceptibility results indicate a magnetically mixed state, composed of paramagnetic domains and SG-type spin domains and (2) the $M(H)$ results indicate predominant AFM-type magnetization curves of the spin clusters. Accordingly, we assume the magnetization to be a sum $M = M_p + M_{AFM}$, where M_p describes the paramagnetic part, while M_{AFM} is an approximation for the cluster part of the magnetization. If the paramagnetic spins would be totally noninteracting, M_p should be written as a sum of four Brillouin functions, each one with its own set of the g and J parameters pertinent to the four RE elements constituting the Ce$_x$PrNdSm alloys and weighted with the respective EDS concentrations of the elements in the alloy. However, at temperatures below the spin freezing transition, it is unphysical to assume that the paramagnetic spins are totally noninteracting (though long-range magnetic ordering does not take place), in which case the Langevin classical theory of paramagnetism appears more suitable. The Langevin theory assumes that each magnetic "particle" can possess an effective magnetic moment of arbitrary magnitude. For a paramagnet with weak interspin interactions, a magnetic particle can be a cluster of a few coupled spins, possessing an effective magnetic moment $\mu_{eff} = p_{eff}\mu_B$ that is by a small factor (such as 2–3) larger than the moments of single ions, accounting for the emerging short-range magnetic order. Consequently, the total magnetization can be written as

$$M = M_p + M_{AFM} = M_0 \mathscr{L}(y) + \chi_{AFM} H \tag{2}$$

Here $\mathscr{L}(y) = \coth y - 1/y$ is the Langevin function, $y = \mu_0 \bar{p}_{eff} \mu_B H / k_B T$, where $\bar{p}_{eff}$ is the mean effective Bohr magneton number of the paramagnetic moments in the regime where the short-range order starts to build, M_0 is the paramagnetic saturation magnetization and χ_{AFM} is the susceptibility of the spin clusters. The fit parameters are M_0, $\bar{p}_{eff}$ and χ_{AFM}. Eq. (2) cannot reproduce the $M(H)$ hysteresis, but just the

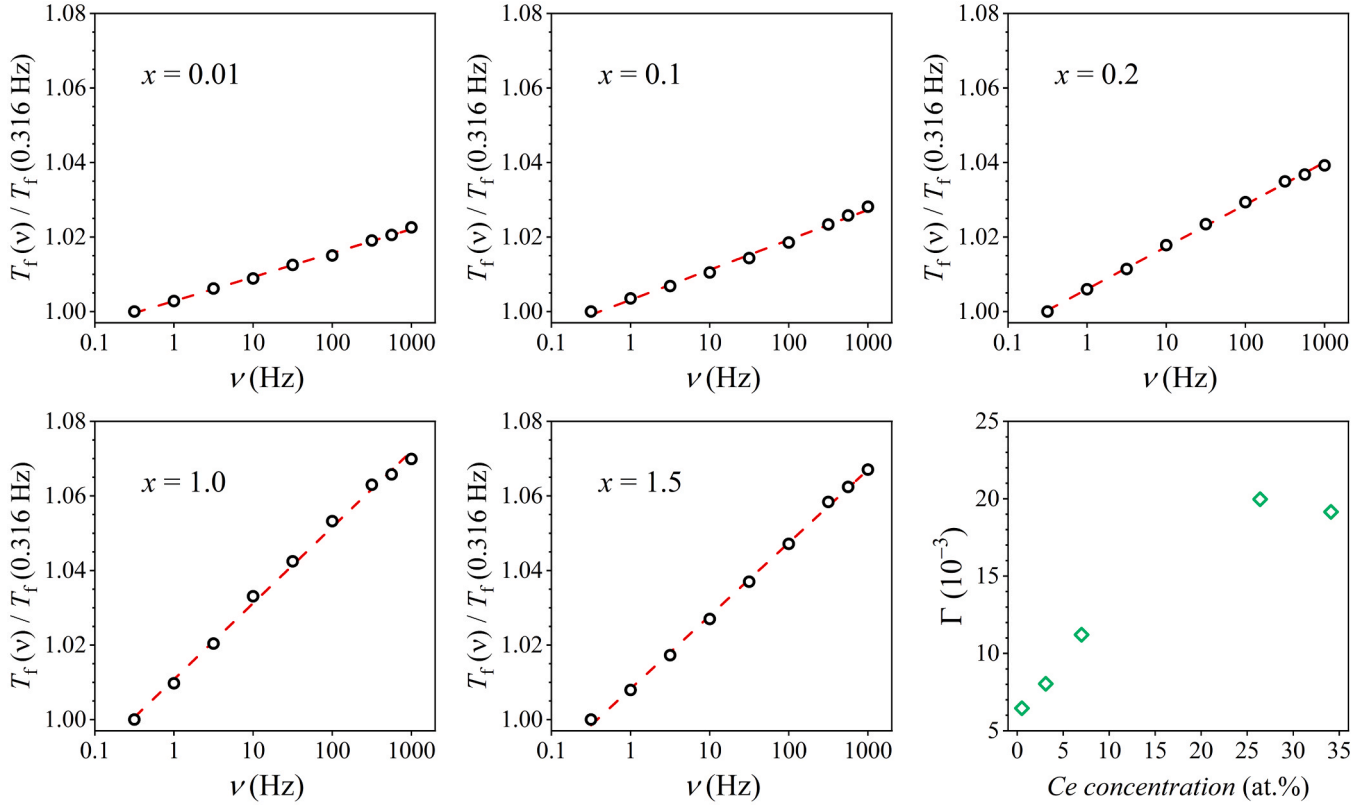

Fig. 12. The relation $T_f(\nu)/T_f(0.316\ \mathrm{Hz})$ on a logarithmic frequency scale for all alloys. The lower right panel shows the fractional shift of the spin freezing temperature per decade of frequency $\Gamma = \Delta T_f/T_f \Delta(\log\nu)$, as a function of the Ce EDS concentration.

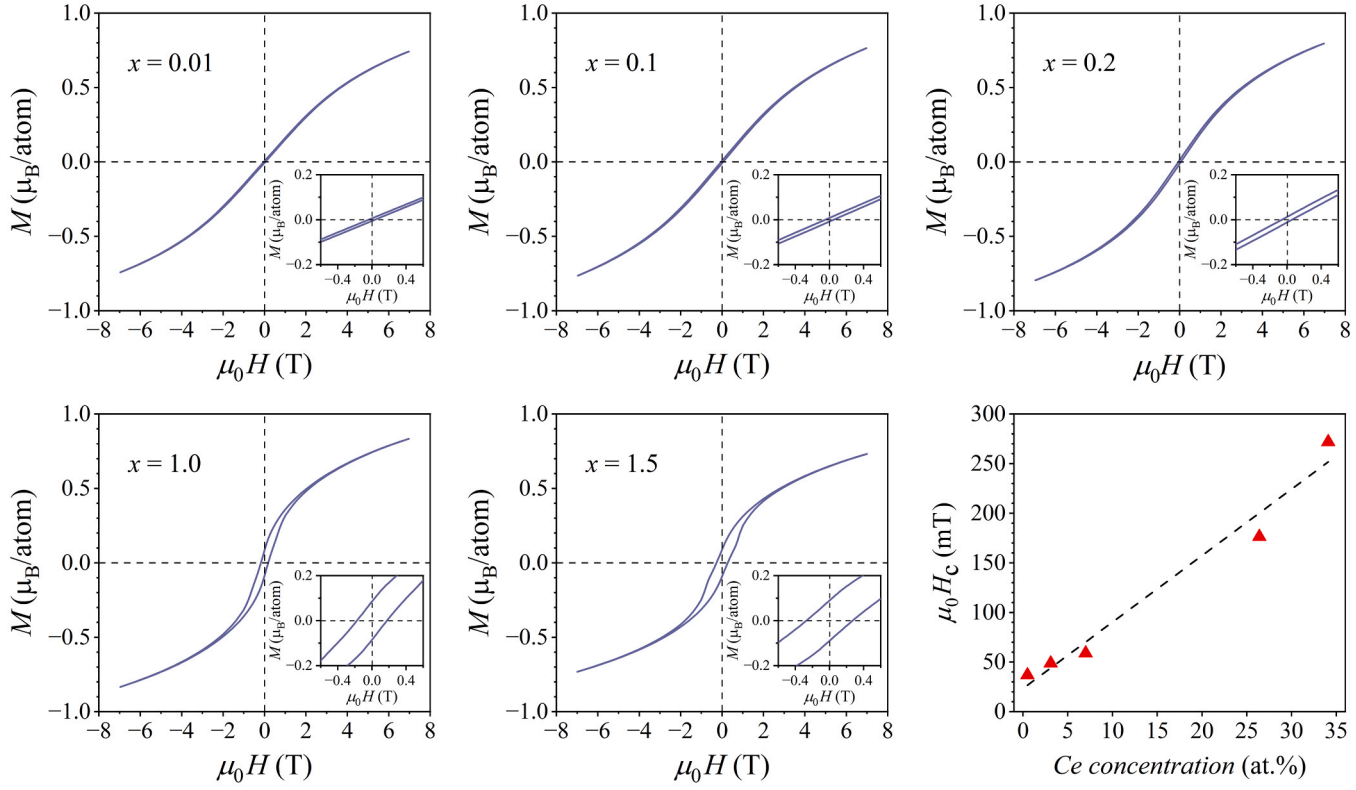

Fig. 13. Magnetization versus magnetic field, $M(H)$, curves of all alloys at the temperature 1.8 K. The hysteresis is presented on an expanded scale in the insets. The magnetization is presented per average atom of the alloy, e.g., per one $Ce_{0.031}Pr_{0.309}Nd_{0.321}Sm_{0.339}$ "atom" in the case of the $x = 0.1$ alloy. The lower right panel shows the coercive field at 1.8 K as a function of the Ce EDS concentration.

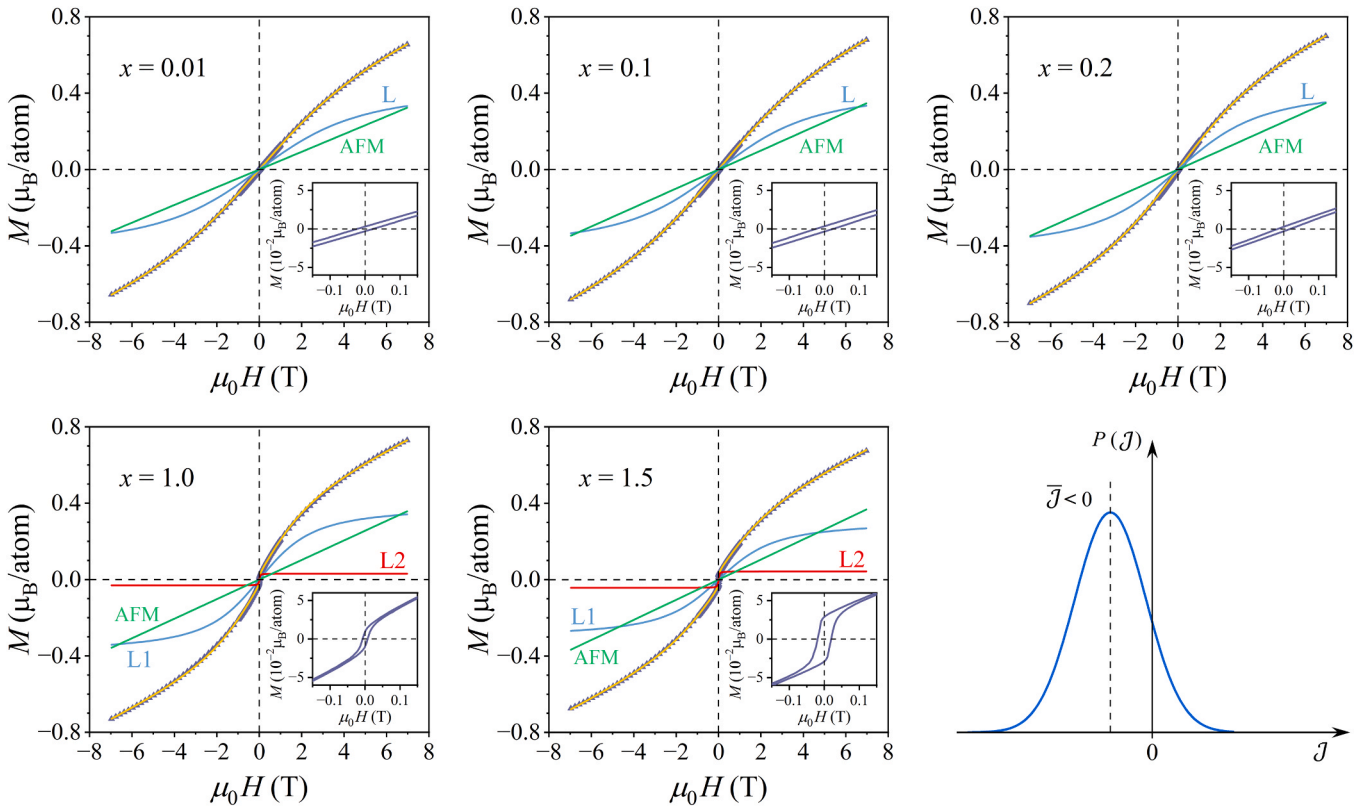

Fig. 14. The $M(H)$ curves of all alloys at 10 K. The inset in each panel shows the particular curve in the low-field region on an expanded scale. Solid curves are fits described in the text. Individual contributions to the total magnetization are also shown, where the antiferromagnetic contribution is denoted as AFM, whereas the Langevin contribution is denoted as L (or L1 and L2 for the two Ce-concentrated alloys). The magnetization is presented per average atom of the alloy, e.g., per one $Ce_{0.031}Pr_{0.309}Nd_{0.321}Sm_{0.339}$ "atom" in the case of the $x = 0.1$ alloy. The distribution function of the exchange constants $P(\mathcal{J})$ for a SG-type system with predominant AFM-type coupling between the spins is shown schematically in the lower right panel.

average trend of the $M(H)$ curve within the hysteretic region. For that reason, we have performed fitting of the $M(H)$ curves at $T = 10$ K, where the hysteresis width is still tiny. Though the Langevin theory cannot account for the hysteresis, it is also widely used in literature to reproduce the average trend of the $M(H)$ curves of FM and FiM materials, by taking large values of the $\overline{p}_{eff}$ parameter, such as 100 or 1000 (depending on the size of the magnetically ordered spin domains).

When constructing the fitting model for the two Ce-concentrated alloys $x = 1.0$ and 1.5, we recall that their experimental $M(H)$ curves exhibit an additional fast-growing magnetization component relative to the three low-Ce content alloys. This additional component can be modeled by a second Langevin term added to Eq. (2), with a much larger value of the $\overline{p}_{eff}$ parameter. The magnetization is then written as $M = M_{01}\mathcal{L}(y_1) + M_{02}\mathcal{L}(y_2) + \chi_{AFM}H$, with two different mean effective Bohr magneton numbers $\overline{p}_{eff,1}$ and $\overline{p}_{eff,2}$ as the fit parameters.

The fits of the 10 K $M(H)$ curves with the theoretical expressions described above are presented as solid curves in Fig. 14. Individual contributions to the total magnetization are also shown, whereas the fit parameters are collected in Table 5. The $\overline{p}_{eff}$ values of the three low-Ce content alloys $x =$ 0.01, 0.1 and 0.2 amount to 8.0, 8.5 and 9.7, respectively, with the estimated uncertainty of ±1. As shown in the lower right panel of Fig. 10, the corresponding high-temperature paramagnetic $\overline{p}_{eff}$ values amount to about 2.9 for all three alloys, so that the $\overline{p}_{eff}$ values below the spin freezing transition are by a factor about 2–3 larger than the theoretical single-ion paramagnetic Bohr magneton numbers $p_{Ce} = 2.54$, $p_{Pr} = 3.58$, $p_{Nd} = 3.62$ and $p_{Sm} = 0.85$ [15]. This justifies the employed assumption that the paramagnetic spins below the spin freezing transition form clusters of a few coupled spins, a precursor of magnetic short-range order. The two Ce-concentrated alloys possess

Table 5
Fit parameters of the $M(H)$ magnetization curves at $T = 10$ K, as presented in Fig. 14. The quantities that are presented *per atom* were calculated per average atom of the alloy, e.g., per one $Ce_{0.031}Pr_{0.309}Nd_{0.321}Sm_{0.339}$ "atom" in the case of the $x = 0.1$ alloy.

Alloy	M_0 (μ_B/atom)	$\overline{p}_{eff}$	χ_{AFM}/μ_0 (μ_B T^{-1}/atom)	M_{01} (μ_B/atom)	$\overline{p}_{eff,1}$	M_{02} (μ_B/atom)	$\overline{p}_{eff,2}$
$x =$ 0.01	0.454	8.0	0.04639				
$x = 0.1$	0.446	8.5	0.04971				
$x = 0.2$	0.452	9.7	0.04992				
$x = 1.0$			0.05125	0.397	15.1	0.031	850
$x = 1.5$			0.05267	0.315	14.5	0.043	864

two different mean effective Bohr magneton numbers each, amounting to $\overline{p}_{eff,1} = 15.1 \pm 1$ and $\overline{p}_{eff,2} = 850 \pm 10$ for the $x = 1.0$ alloy and $\overline{p}_{eff,1} = 14.5 \pm 1$ and $\overline{p}_{eff,2} = 864 \pm 10$ for $x = 1.5$. The $\overline{p}_{eff,1}$ values are slightly increased with respect to those of the three low-Ce content alloys (by a factor less than 2), indicating somewhat increased magnetic short-range order within the paraphase. On the other hand, the large $\overline{p}_{eff,2} \approx 860$ values reveal the presence of giant local magnetic moments, attributable to large spin clusters.

We also comment the meaning of the employed approximation that the magnetization of the SG-type domains was modeled by the AFM-type expression $M_{AFM} = \chi_{AFM}H$. In a SG, randomness introduces a continuous distribution $P(\mathcal{J})$ of the exchange coupling constants $\mathcal{J}$. For a SG system with predominant AFM-type couplings, the average interaction is biased towards a net negative value, $\overline{\mathcal{J}} < 0$, at which the $P(\mathcal{J})$ is peaked (shown schematically in the lower right panel of Fig. 14). The employed

approximation is thus equivalent of replacing the $P(\mathcal{J})$ distribution by a single average $\overline{\mathcal{J}} < 0$ coupling constant.

4.5. Electrical resistivity

Electrical resistivity $\rho(T)$ was determined at temperatures between 300 and 1.8 K in magnetic fields $\mu_0 H = 0$–9 T. The zero-field resistivities of all alloys normalized to their RT values, $\rho(T)/\rho_{300K}$, are shown in Fig. 15 (lower right panel), whereas the raw data (not normalized) are shown in Fig. S8 of the Supplementary material. The raw data are affected by the experimental error coming from the uncertainty in the determination of the samples' length and cross section and possible inhomogeneity of the electrical contacts. This error makes the absolute resistivity values of different samples to scatter randomly (uncorrelated to the Ce content x) by about ±5 % around the average value that amounts at RT to about 80 μΩcm. When analyzing the normalized resistivity $\rho(T)/\rho_{300K}$, these errors are compensated and the dependence on the Ce content becomes evident. The resistivities are metallic-type, with a linear increase at temperatures above about 100 K, where the positive temperature coefficient gradually decreases with increasing Ce content x. Below 100 K, the variation of $\rho(T)$ becomes stronger and the resistivity starts to depend on the magnetic field below about 40 K. This is demonstrated in other panels of Fig. 15, where the resistivities in the fields 0, 3, 6 and 9 T are shown on an expanded temperature scale, in a separate panel for each alloy. The resistivity decreases with increasing field, which can be explained by considering that the total resistivity is a sum $\rho = \rho_{imp} + \rho_{ph} + \rho_m$, where ρ_{imp} is a temperature-independent term due to elastic scattering of conduction electrons by quenched impurities (including static lattice distortions), ρ_{ph} is a temperature-dependent term due to electron-phonon scattering that increases with temperature as T^n (where $n = 1$ well above the Debye temperature and $n = 3$–5 far below it), whereas ρ_m is a temperature-dependent magnetic contribution known as spin-disorder scattering, which is especially pronounced in RE metals and alloys. The origin of ρ_m is inelastic scattering of the conduction electrons by the thermally-induced excitations of the magnetic state or fluctuations of short-range ordered magnetic clusters on approaching the collective state. Coupling of the fluctuating RE moments to the conduction electrons induces electronic transitions from an occupied state $\left|\vec{k}\,\sigma\right\rangle$ to an unoccupied state $\left|\vec{k}\,'\sigma'\right\rangle$, where $\vec{k}$ is the wave vector and σ the spin of conduction electron, which is the microscopic mechanism of ρ_m. In an increasing magnetic field, the growing Zeeman interaction locks and holds the fluctuating moments along the field direction and impedes their reorientations, so that the magnetic contribution ρ_m to the electrical resistivity is reduced.

The shape of the $\rho(T)$ curves in the low-temperature regime, where they depend on the magnetic field deserves special attention. For the alloy with the lowest Ce content $x = 0.01$, the $\rho(T)$ curves do not show any peculiarity, while in the alloys with increasing x, the curves gradually undergo a transition to a region with a significantly larger (positive) slope in the low-temperature limit. This is indicated by an arrow in the resistivity graphs of the two Ce-concentrated alloys in Fig. 15. Such behavior is characteristic for magnetic structures with nonzero spontaneous magnetization (FM and FiM states), where the spin-disorder resistivity is given by $\rho_m = \rho_{para}\left\{1 - [M(T)/M(0)]^2\right\}$ [27–29]. Here M is the spontaneous magnetization of the FM or FiM state that is nonzero below the magnetic ordering temperature, either Curie temperature T_C for a FM or Néel temperature T_N for a FiM, but also slightly above those temperatures due to the development of the magnetic short-range order within the paramagnetic phase. The term ρ_{para} is the magnetic resistivity of the paramagnetic state that is temperature independent and proportional to the square of the exchange coupling constant between the localized spins and the conduction electrons. The above ρ_m expression gives a rather discontinuous change of slope in the total $\rho(T)$ when crossing the transition temperature. Applying the magnetic field, M is increased, which produces negative magnetoresistance. All this is consistently observed in the experimental resistivity curves of Fig. 15. For the $x = 1.0$ and 1.5 alloys, the transition to the nonzero spontaneous magnetization state (in a fraction of the sample) occurs in the vicinity of 10 K, in agreement with the dc susceptibility results.

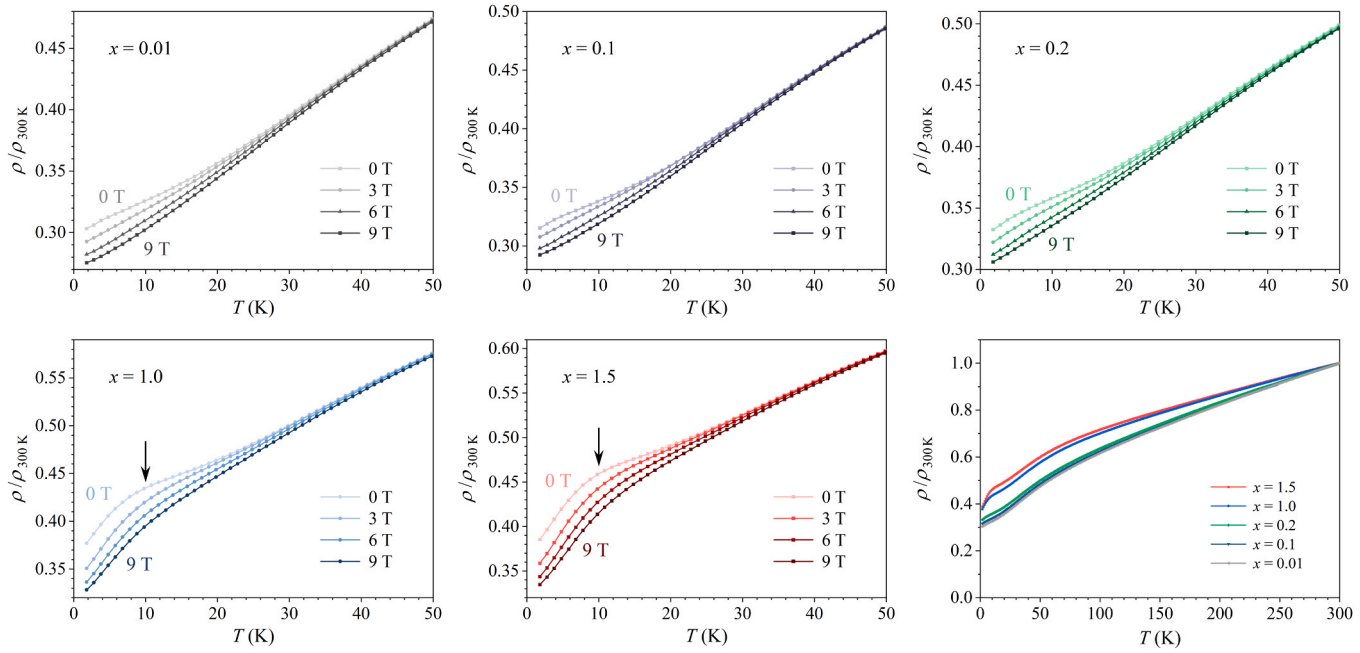

Fig. 15. Electrical resistivities $\rho(T)/\rho_{300K}$ of all alloys in the low-temperature range below 50 K in magnetic fields 0, 3, 6 and 9 T. The arrows in the graphs of the $x =$ 1.0 and 1.5 alloys indicate the temperature of the rather discontinuous change of slope of the total $\rho(T)$ when crossing the transition temperature, where a spontaneous-magnetization state in a part of the sample develops. The lower right panel shows the normalized resistivities $\rho(T)/\rho_{300K}$ of all alloys in zero magnetic field in the entire investigated temperature range 1.8–300 K.

4.6. Magnetoresistance

The magnetoresistance $[\rho(H)-\rho(0)]/\rho(0) = \Delta\rho/\rho$ is another suitable physical quantity to characterize the type of the magnetic state. The magnetoresistance curves of the $Ce_xPrNdSm$ alloys were measured in the temperature range 300–2 K in a magnetic field sweep $\mu_0 H = \pm 9$ T. The $\Delta\rho/\rho$ curves of all alloys in the entire field sweep are presented in Fig. 16, while expanded portions of the curves in the field sweep ±2 T are shown in the insets. The $\Delta\rho/\rho$ curves of the three low-Ce content alloys are negative at any temperature in the entire field sweep. The two Ce-concentrated alloys behave differently. While their $\Delta\rho/\rho$ curves at temperatures between RT and about 10 K are negative in the entire field sweep, this behavior changes in the low-temperature limit $T < 10$ K, where upon applying the field, the magnetoresistance in the low-field regime from zero up to about 0.5 T (depending on temperature) is positive and increases with the field, passes through a maximum and then turns into a negative magnetoresistance at higher fields.

Theoretical mean-field considerations predict that the magnetoresistance of paramagnetic and FM states is negative, going quadratically with the field for a paramagnet, $\Delta\rho/\rho \propto -H^2$, while for the FM state $\Delta\rho/\rho \propto -H^{2/3}$ at temperatures close to the FM transition ($T \approx T_C$) that gradually evolves into a linear dependence $\Delta\rho/\rho \propto -H$ below T_C [30]. As already discussed, the negative sign of the magnetoresistance is a consequence of the suppression of the moments' thermal fluctuations by the external magnetic field. The situation is different for the AFM and FiM structures [31]. Considering a simple Néel-type antiferromagnet with two equal, but oppositely polarized spin sublattices, and assuming that the magnetic field is applied along one of the sublattice polarizations, the magnetic field impedes thermal fluctuations of spins on the sublattice polarized along the field, while the spin fluctuations of the oppositely polarized sublattice are increased, because the external field tries to flip those spins into the field direction to minimize their Zeeman energy. Accordingly, the magnetoresistance is positive and increases with the field. At the spin-flop field H_{sf}, the oppositely polarized sublattice rotates into the field direction, and further increase of the field then impedes thermal fluctuations of both sublattices, resulting in a negative magnetoresistance like for the ferromagnet and paramagnet. The magnetoresistance consequently shows a maximum at H_{sf}. The situation for a ferrimagnet is analogous, because a Néel-type FiM structure can be visualized in the same way as the Néel-type AFM, with the difference that the two sublattice magnetizations are unequal, leading to a nonzero spontaneous magnetization of the ordered state. Since only the two Ce-concentrated alloys $x = 1.0$ and 1.5 show the "anomalous" magnetoresistance, and the $M(H)$ analysis reveals that these two alloys contain spin clusters with giant local magnetic moments, we infer that these clusters must be FiM-ordered. The maxima in the magnetoresistance can then be associated with the temperature-dependent spin-flop field (amounting at $T = 2$ K to $\mu_0 H_{sf} = 0.65$ T for the $x = 1.5$ alloy and $\mu_0 H_{sf} \approx 0.4$ T for $x = 1.0$). The temperature-dependent spin-flop field $H_{sf}(T)$ of these two alloys is shown in the lower right panel of Fig. 16.

5. Discussion

In discussing the type of magnetic state and its evolution with the cerium content x in the $Ce_xPrNdSm$ MEAs, we first review the magnetic structures of pure metals of the constituent elements. The magnetism of the Ce, Pr, Nd and Sm metals is highly complex, emphasizing the important role of the CF interaction [15]. The CF energy-level scheme of the triply ionized RE ions follows the Kramers' theorem, which states that the energy levels of ions with an odd number of electrons, and therefore half-integral quantum numbers, are always at least two-fold degenerate in the absence of a magnetic field. When J is half-integral, the quadrupole part of the CF interaction produces a series of Kramers' doublets $|\pm M_J\rangle$, but when J is integral, there is a singlet $|0\rangle$ and a series of doublets. The doublets carry magnetic moments, while the singlet state, in common with all singlet states, carries no moment. When the $M_J = 0$ singlet is the ground state, the crystal fields have destroyed the moment and there is no magnetism in the low-temperature limit. If, however, the ground state is $|\pm J\rangle$, the crystal fields cannot suppress magnetic ordering but they reduce the ordered moment and contribute to the complexity of the magnetic structures. External magnetic field changes the energy levels and a new set of single-ion levels is obtained by diagonalizing the sum of the CF and Zeeman Hamiltonians, $\mathscr{H}_{CF} + \mathscr{H}_Z$, which are then used to evaluate the thermodynamic average magnetic moment of the ion. Bulk magnetic structures of the light-RE

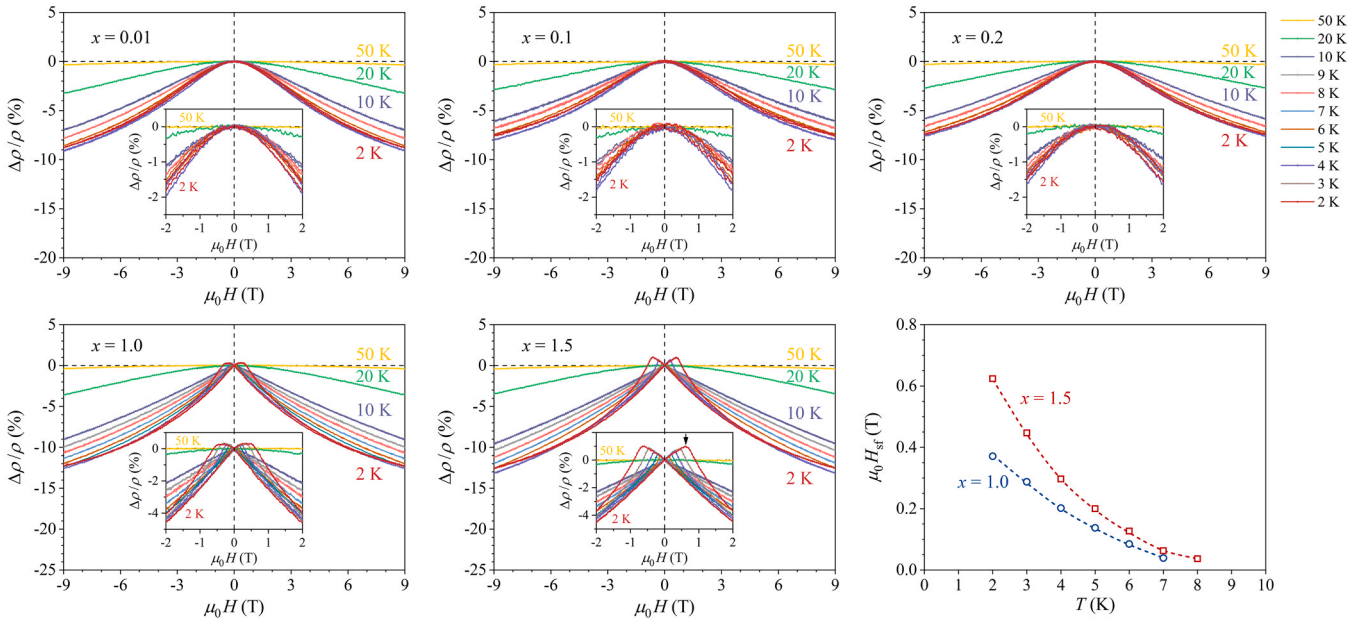

Fig. 16. Magnetoresistance curves of the $Ce_xPrNdSm$ alloys at different temperatures in a magnetic field sweep $\mu_0 H = \pm 9$ T. The insets show expanded portions of the curves in the field sweep ±2 T. The arrow at the maximum of the 2 K $\Delta\rho/\rho$ curve in the inset of the $x = 1.5$ alloy panel marks the spin-flop field. The lower right panel shows the temperature-dependent spin-flop field $H_{sf}(T)$ of the $x = 1.0$ and 1.5 alloys.

metals are further aggravated by the two different site symmetries (hexagonal and cubic) in the dhcp lattice.

The triply ionized Ce, Pr, Nd and Sm ions are distinguished by their total angular momentum quantum number, which is integral for Pr ($J = 4$), but half-integral for Ce, Nd and Sm ($J = 5/2$ for Ce and Sm and $J = 9/2$ for Nd). Having integral J, Pr is the most remarkable example of the influence of CFs on the magnetism of the metallic state [32,33], because CFs are able to frustrate the efforts of the exchange to produce a magnetically ordered state. Due to the negative sign of the electric field gradient, the ground state on the hexagonal sites in Pr is the $|0\rangle$ singlet, which carries no moment. In a magnetic field, higher-energy doublet states are mixed into the ground state, creating a magnetic moment. If the exchange would be strong enough, magnetic ordering would result; otherwise paramagnetism persists down to absolute zero. In Pr, the CF splitting is strong enough to preclude magnetic ordering, but the exchange is over 90 % of that required for antiferromagnetism. Experimentally, it was reported that the moments at the hexagonal sites of Pr still order AFM at a very low temperature $T_N = 0.05$ K, while no ordering was reported for the cubic sites.

The Ce, Nd and Sm ions have an odd number of 4 f electrons, and according to the Kramers' theorem, the CF levels are doublets that carry a magnetic moment. The CFs cannot suppress magnetic ordering, but they reduce the saturation moment below the theoretical $gJ\mu_B$ value [34]. The magnetic structure of β-Ce metal (dhcp) has been described by commensurate transverse waves that are formed on both hexagonal and cubic sites, with the wave vector $\vec{q}$ in the b-direction of the dhcp structure and the moments pointing along the a-axis in the plane [35]. The magnetic periodicity is double that of the lattice. The AFM Néel temperature of the hexagonal sites is 13.7 K, while the moments at the cubic sites order AFM at 12.5 K. The CFs drastically reduce the saturation moment of Ce from the theoretical value $2.14\mu_B$ to the experimental value $0.6\mu_B$. The Nd metal, on the other hand, displays an extraordinarily complex magnetic structure [36,37]. An incommensurate longitudinal wave in a b-direction is formed on the hexagonal sites through a first-order AFM transition at $T_N = 19.9$ K, with a simple AFM arrangement of successive hexagonal layers. Upon lowering the temperature, another first-order transition takes place within a degree to a double-$\vec{q}$ structure. At $T_N = 8.2$ K, an incommensurate periodic structure in the b-direction is formed also on the cubic sites. At the lowest temperatures, the moments arrange in an elaborate quadruple-$\vec{q}$ pattern. In Sm, the hexagonal sites order AFM at $T_N = 106$ K, with the magnetic structure comprising pairs of planes with the moments arranged ferromagnetically in the c-direction [38]. Adjacent pairs are coupled AFM and separated by the cubic sites. The latter also order AFM at $T_N = 14.0$ K, with the moments along the c-axis, but the normal to the FM sheets is now in the (b,c) plane.

The experimental results presented in this work reveal that the low-temperature magnetic state of the Ce_xPrNdSm MEAs is inhomogeneous, appearing as a mixture of paramagnetic spin domains and spin domains (clusters) with stronger coupled spins. The coupling is predominantly AFM, which is not surprising because the pure metals are all AFM. The clusters are magnetically frustrated and show broken-ergodicity phenomena, such as the zfc–fc dc susceptibility splitting in low magnetic fields and the frequency-dependent peak in the ac susceptibility. This indicates that the magnetic ordering within the clusters is of a SG-type with predominant AFM coupling [39]. In the three low-Ce content alloys $x = 0.01$, 0.1 and 0.2, the SG-type clusters do not show any spontaneous magnetization, resembling canonical SGs, while in the two Ce-concentrated alloys $x = 1.0$ and 1.5, some FiM-ordered spin clusters with nonzero spontaneous magnetization have formed in addition. The increased Ce content x in the Ce_xPrNdSm MEA series reduces the average exchange coupling, as evidenced from the shift of the spin freezing temperature T_f towards lower temperatures and the speed-up of the spin dynamics from SG-type into the direction of superparamagnets (though the superparamagnetic limit is not reached). These results raise the following fundamental questions:

(1) Is the inhomogeneous (mixed) magnetic state in the Ce_xPrNdSm MEAs intrinsic to the light-RE spin system when the alloys are in the form of an ideal solid solution with random distribution of the four RE elements? A related question is whether the magnetic frustration and broken ergodicity of the spin clusters are intrinsic properties of the Ce_xPrNdSm solid solutions?
(2) Why does the increased Ce content in the Ce_xPrNdSm MEAs result in a reduction of the average exchange coupling between the magnetic moments?
(3) Why were some FiM-ordered spin clusters detected only in the two Ce-concentrated alloys $x = 1.0$ and 1.5, but not also in the low-Ce content alloys?

Discussing the question (1), we first note that the Ce_xPrNdSm MEAs are magnetically concentrated alloys with all sites of the dhcp lattice populated by magnetic elements. We consider that the alloys are random solid solutions, with the four different types of magnetic moments distributed statistically over the lattice sites. Randomness introduces continuous probability distributions of the RKKY exchange coupling constant and the magnetocrystalline anisotropy. Since the RKKY exchange is long-range, involving many shells of interacting spins, and the interaction changes sign between positive and negative with the inter-spin distance r on the scale of nanometers, the resulting spin state is magnetically frustrated, with broken ergodicity at low temperatures. This consideration insinuates that the entire spin system in the Ce_xPrNdSm MEAs should behave at low temperatures spin glass-like and would be hence magnetically homogeneous. However, the CF interaction that is randomly changing over the lattice sites may either reduce or completely destroy some localized ionic magnetic moments at low temperatures and preclude the efforts of the exchange to produce magnetic ordering. The resulting magnetic state is then inhomogeneous, consisting of paramagnetic domains appearing in the crystal regions with larger destruction of the moments and SG-type spin domains in the regions with less destructed moments. Such mixed state is intrinsic to an ideal random solid solution of the light-RE elements and does not require any structural disorder or chemical inhomogeneity. It is also specific to the light-RE multi-component solid solutions only, because of the decisive role of the CF interaction that is able to reduce or completely destroy the moments, in addition to establishing their directions in the lattice. This is different from the heavy-RE multi-component solid solutions, where the CF effects are relatively weaker in comparison to the exchange, with their main role being merely to establish favored directions for the moments in the crystal. For the heavy-RE HEAs, such mixed magnetic state has not been reported in literature, supporting this hypothesis.

The question (2) why does the average exchange coupling decrease with the increased Ce content can be elucidated by the following considerations. In a metallic environment, the localized 4 f RE moments interact indirectly via the 5d/6 s conduction electrons and the effective coupling between two localized spins $\vec{S}$ separated by a distance r is $\mathcal{J}_{eff} \approx 9\pi\mathcal{J}_{sf}^2 z^2 F(\xi)/(64\varepsilon_F)$ [40]. Here, $\mathcal{J}_{sf}$ is the sf exchange integral, z is the number of conduction electrons per atom, $F(\xi) = (\sin\xi - \xi\cos\xi)/\xi^4$ is the RKKY oscillatory function with $\xi = 2k_F r$ (where k_F is the Fermi wavevector) and ε_F is the Fermi energy. Among the triply ionized RE ions, only gadolinium (Gd) has the spin S as a good quantum number, while the others have the total angular momentum J as their quantum number. Yet the exchange interaction couples spins, so that one needs to project $\vec{S}$ onto $\vec{J}$ when calculating the exchange coupling between two RE ions 1 and 2 from the Hamiltonian $\mathcal{H}_{RKKY} = -\mathcal{J}_{RKKY}\vec{J}_1 \bullet \vec{J}_2$. For two like ions ($g$,$J$), this introduces the de Gennes factor G into the RKKY exchange coupling constant $\mathcal{J}_{RKKY} = G\mathcal{J}_{eff}$ with $G = (g-1)^2 J(J+1)$, while for two unlike ions (g_i, J_i) and $\left(g_j, J_j\right)$, the de Gennes factor is

modified to $G_{ij} = (g_i - 1)\left(g_j - 1\right)\sqrt{J_i(J_i+1)J_j(J_j+1)}$ [6,40]. It is known that the magnetic ordering temperatures of any series of RE metals or compounds with the same electronic band structure and similar lattice spacing scale with G (or G_{ij}), originating from the scaling of the $\mathcal{J}_{RKKY}$ coupling constant. In the Ce$_x$PrNdSm MEAs, the four kinds of RE ions all experience the same band structure and lattice spacing, so it is straightforward to assume that the RKKY coupling between any pair of ions i and j (i,j = Ce, Pr, Nd, Sm) obeys the relation $\mathcal{J}^{ij}_{RKKY} = G_{ij}\mathcal{J}_{eff}$. Using the g and J values from Table 4, we have calculated the G_{ij} factors for all like and unlike pairs and the results are presented graphically in Fig. 17. The G_{ij} distribution spans from G_{SmSm} (the largest) to G_{CeCe} (the weakest, amounting to 4 % of the G_{SmSm} only). The G_{ij} factors of Ce to any other ion are among the smallest, explaining why the average RKKY coupling strength in the Ce$_x$PrNdSm MEAs is continuously reduced with the increasing Ce content x.

The question (3) why were some FiM-ordered spin clusters detected only in the Ce-concentrated alloys, but not also in the low-Ce content ones is more subtle and cannot be answered satisfactorily based of the presented experimental results. In the Ce$_x$PrNdSm random solid solutions, the four types of RE ions possess different magnetic moments, which in addition depend on the type of site (hexagonal or cubic) in the dhcp lattice. The FiM state by definition possesses nonzero spontaneous magnetization, despite the antiparallel arrangement of the moments. This requires that at least two magnetic sublattices can be defined on a chemical basis, where the two sublattice magnetizations are oppositely polarized and of different magnitude. In disordered magnetic metallic alloys with random distribution of the chemical elements, a FiM-type magnetic state is known in the context of amorphous magnets, where it is termed the *sperimagnetic* state [40]. The presence of the FiM spin fraction in the two Ce-concentrated Ce$_x$PrNdSm alloys is clearly manifested experimentally by the magnetoresistance that changes sign from positive to negative upon increasing the magnetic field. The fact that the FiM clusters form only in the Ce-concentrated Ce$_x$PrNdSm alloys then suggests that this may be another effect of cerium, possibly in relation to the two types of sites in the dhcp lattice. Further investigations are needed to elucidate this open question.

6. Conclusions

While the studies of HEAs composed of the RE elements from the heavy half of the lanthanide series (from Gd to Lu) are numerous in literature, the HEAs and MEAs composed of the light-RE lanthanides were not reported in literature as yet, to the best of our knowledge. The fundamental difference between the light- and heavy lanthanides originates in the CF interaction, which in the heavy-RE alloys is weak enough to act just as a perturbation to the exchange interaction, with its main role being to establish favored directions for the moments in the crystal. In contrast, in the light-RE alloys, the CF interaction is considerably stronger relative to the exchange and is able to reduce or completely destroy the magnetic moments at low temperatures, in addition to establishing their directions in the crystal. In this paper, we have presented a study of the structure, microstructure, nanostructure and magnetic state of the light-RE MEA series Ce$_x$PrNdSm with the nominal Ce contents in the range x = 0.01–1.5. All investigated compositions crystallize in the dhcp structure in the form of a single-phase random solid solution. The low-temperature magnetic state is inhomogeneous, being a mixture of paramagnetic domains appearing in the crystal regions with larger destruction of the moments and SG-type spin domains in the regions with less destructed moments. Such mixed state is intrinsic to an ideal random solid solution of the light-RE elements and also specific to the light-RE multi-component solid solutions only, because of the decisive role of the CF interaction. The SG-type domains are magnetically frustrated spin entities with broken ergodicity on the experimental time scale below the spin freezing temperature T_f. In the three low-Ce content alloys x = 0.01, 0.1 and 0.2, the SG-type domains resemble canonical SGs with zero spontaneous magnetization, while in the two Ce-concentrated alloys x = 1.0 and 1.5, some FiM-ordered spin clusters with nonzero spontaneous magnetization have formed additionally. The increased Ce content x in the Ce$_x$PrNdSm MEA series continuously reduces the average exchange coupling, as evidenced from the shift of the spin freezing temperature T_f towards lower temperatures and the speed-up of the spin dynamics from SG-type into the direction of superparamagnets.

The presented magnetic study of the Ce$_x$PrNdSm MEAs is experimental, based on the measurements of the dc and ac magnetic susceptibility, $M(H)$ magnetization curves and magnetoresistance. The results are discussed at a qualitative level, while a quantitative theoretical analysis of the magnetic state is still lacking. This is not surprising, as even the magnetic structures of the light-RE pure metals are currently reasonably well described only phenomenologically, while their theoretical explanations are still at a rudimentary stage [15]. The main difficulties encountered in a quantitative theoretical treatment are (1) two types of crystallographic sites (hexagonal and cubic) in the dhcp lattice that result in two kinds of CF interactions, (2) comparable magnitudes of the exchange, CF and Zeeman interactions, where the full Hamiltonian including all three terms needs to be diagonalized to obtain spin energy levels and (3) the immense random chemical disorder in the multi-component solid solution.

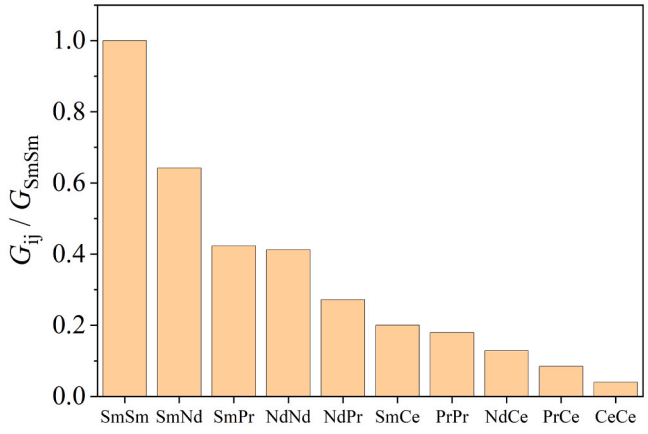

Fig. 17. The de Gennes factor G_{ij} normalized to G_{SmSm} for all ten atomic pairs (like and unlike) of the elements Ce, Pr, Nd and Sm.

7. Experimental section

XRD diffraction patterns were collected in reflection mode using PANalytical X'Pert PRO MPD X-ray powder diffractometer equipped with a primary Ge monochromator, delivering pure Cu Kα_1 radiation (λ = 1.54056 Å), and X'Celerator position-sensitive detector.

SEM BSE imaging and EDS chemical composition determination and elemental mapping were performed by the scanning electron microscope ThermoFisher Quanta 650 ESEM equipped with EDS Oxford Instruments AZtec Live, Ultim Max SDD 40 mm^2. The surfaces were prepared by the FEI FIB Helios NanoLab 650 dual-beam system using gallium ions.

HAADF and BF STEM imaging and EDS analysis, as well as SAED study were performed by a Cs-corrected Jeol ARM 200 CF STEM microscope equipped with an SDD Jeol Centurio energy-dispersive X-ray spectrometer. The operating voltage was set to 200 kV. The lamellae were prepared by the FIB Helios NanoLab 650 FEI dual-beam system using gallium ions via the following protocol. The sample and the FIB lift-out grid were mounted into a CleanConnect capsule inside an Ar-filled glovebox and transferred in Ar 5.0 overpressure (200 mbar) directly to the FIB instrument. The sample surface was initially protected

by a 500 nm Pt layer using electron beam induced deposition (EBID, 2 kV at 0.4 nA). Subsequently, an additional Pt layer was deposited using Ga+ ion beam induced deposition (IBID, 30 kV at 0.23 nA) to achieve a protective layer with a final thickness of 1.8 μm. A lamella chunk with dimensions of 12 × 6 μm^2 was thinned to 2 μm and transferred to the FIB grid using a micromanipulator. Due to the sample's sensitivity, the lamella was first thinned to 250 nm thickness using FIB at 30 kV by sequentially reducing ion beam currents from 780 pA to 80 pA. Subsequently, the lamella was carefully thinned to 100 nm using FIB at 16 kV with a 24 pA beam current. Afterwards, the lamella was sequentially polished on both sides using FIB at 5 kV@44 pA, 2 kV@25 pA, and 1 kV@20 pA until electron transparency (~100 nm) was achieved. The prepared lamella was transferred with the CleanConnect capsule back to the glovebox, where it was mounted to the TEM vacuum transfer holder.

Magnetic measurements were conducted on a Quantum Design MPMS3 SQUID magnetometer equipped with a 7 T magnet, operating at temperatures between 1.8 and 400 K. The samples for measurements were needle-shaped, with the long dimension of 4 mm and the perpendicular dimension of 0.5 mm. The long dimension was set into the direction of the external magnetic field. The demagnetization effect was estimated by approximating the samples' shape with a rotational ellipsoid, having the aspect ratio of the major axes $\alpha = 8$. Using Eq. (2.36a) of ref. [40], the demagnetizing factor was calculated as $\mathcal{N} \approx 0.03$, which is close enough to zero that the demagnetization correction is unimportant and was not applied to the measurements.

Electrical resistivity and magnetoresistance measurements were performed on a Quantum Design Physical Property Measurement System PPMS 9 T. For the resistivity measurements, rectangular bar-shaped samples of dimensions 1 × 1 × 8 mm^3 were used, with the long dimension oriented along the magnetic field direction to minimize the demagnetization effects.

CRediT authorship contribution statement

Julia Petrović: Investigation, Formal analysis, Data curation. **Stanislav Vrtnik:** Validation, Investigation, Data curation. **Andreja Jelen:** Visualization, Investigation. **Primož Koželj:** Supervision, Investigation. **Jože Luzar:** Visualization, Investigation. **Peter Mihor:** Investigation, Formal analysis. **Gregor Kapun:** Investigation. **Goran Dražić:** Validation, Methodology, Investigation. **Anton Meden:** Writing – review & editing, Investigation, Formal analysis, Conceptualization. **Pascal Boulet:** Writing – review & editing, Resources, Methodology, Investigation, Conceptualization. **Janez Dolinšek:** Writing – original draft, Validation, Methodology, Funding acquisition, Formal analysis, Conceptualization.

Declaration of Competing Interest

The authors declare that they have no known competing financial interests or personal relationships that could have appeared to influence the work reported in this paper.

Acknowledgements

This work was performed within the frame of the project MATERIOMICS, conducted jointly by the CNRS Université de Lorraine, F-54000 Nancy, France, and the Jožef Stefan Institute, SI-1000 Ljubljana, Slovenia. The Slovenian authors acknowledge the financial support from the Slovenian Research and Innovation Agency (Research Core Fundings No. P1–0125 and P1–0175 and Project No. N1–0330). All authors thank dr. Vincent Fournée from CNRS Université de Lorraine Nancy for provision of pure rare-earth metals for the samples' synthesis.

Appendix A. Supporting information

Supplementary data associated with this article can be found in the online version at doi:10.1016/j.mtcomm.2026.114898.

Data Availability

Data will be made available on request.

References

[1] M. Feuerbacher, M. Heidelmann, C. Thomas, Hexagonal high-entropy alloys, Mat. Res. Lett. 3 (2014) 1–6.
[2] A. Takeuchi, K. Amiya, T. Wada, K. Yubuta, W. Zhang, High-entropy alloys with a hexagonal close-packed structure designed by equi-atomic alloy strategy and binary phase diagrams, JOM 66 (2014) 1984–1992.
[3] J. Lužnik, P. Koželj, S. Vrtnik, A. Jelen, Z. Jagličić, A. Meden, M. Feuerbacher, J. Dolinšek, Complex magnetism of Ho-Dy-Y-Gd-Tb hexagonal high-entropy alloy, Phys. Rev. B 92 (2015) 224201.
[4] S. Vrtnik, J. Lužnik, P. Koželj, A. Jelen, J. Luzar, Z. Jagličić, A. Meden, M. Feuerbacher, J. Dolinšek, Disordered ferromagnetic state in the Ce-Gd-Tb-Dy-Ho hexagonal high-entropy alloy, J. Alloy. Compd. 742 (2018) 877–886.
[5] S. Vrtnik, J. Lužnik, P. Koželj, A. Jelen, J. Luzar, M. Krnel, Z. Jagličić, A. Meden, M. Feuerbacher, J. Dolinšek, Magnetic phase diagram and magnetoresistance of Gd–Tb–Dy–Ho–Lu hexagonal high-entropy alloy, Intermetallics 105 (2019) 163–172.
[6] M. Krnel, S. Vrtnik, A. Jelen, P. Koželj, Z. Jagličić, A. Meden, M. Feuerbacher, J. Dolinšek, Speromagnetism and asperomagnetism as the ground states of the Tb-Dy-Ho-Er-Tm "ideal" high-entropy alloy, Intermetallics 117 (2020) 106680.
[7] A. Jelen, J.H. Jang, J. Oh, H.J. Kim, A. Meden, S. Vrtnik, M. Feuerbacher, J. Dolinšek, Nanostructure and local polymorphism in "ideal-like" rare-earths-based high-entropy alloys, Mater. Charact. 172 (2021) 110837.
[8] Y. Yuan, Y. Wu, X. Tong, H. Zhang, H. Wang, X.J. Liu, L. Ma, H.L. Suo, Z.P. Lu, Rare-earth high-entropy alloys with giant magnetocaloric effect, Acta Mater. 125 (2017) 481–489.
[9] J.W. Qiao, M.L. Bao, Y.J. Zhao, H.J. Yang, Y.C. Wu, Y. Zhang, Rare-earth high entropy alloys with hexagonal close-packed structure, J. Appl. Phys. 124 (2018) 195101.
[10] I.S. Sipatov, O.A. Korolev, E.V. Ignatieva, L.A. Marshuk, B.R. Gelchinskiy, A. A. Rempel, Mechanical properties of high entropy alloys based on rare earth elements with yttrium and scandium, Phys. Met. Metallogr. 124 (2023) 1303–1310.
[11] H. Fu, Y. Jiang, M. Zhang, Z. Zhang, W. Liang, S. Wang, Y. Du, C. Yan, High-entropy rare earth materials: synthesis, application and outlook, Chem. Soc. Rev. 53 (2024) 2211–2247.
[12] L. Xue, L. Shao, B. Zhang, Z. Li, J. Cheng, B. Shen, Magnetic behaviors and magnetocaloric effects in rare earth high-entropy amorphous/nanocrystalline alloys, J. Rare Earths 42 (2024) 129–136.
[13] J. Ledieu, K. Dumesnil, M. Emo, S. Migot, S. Semsari Parapari, S. Šturm, P. Koželj, V. Fournée, Epitaxial growth of rare-earth high-entropy alloy thin films, ACS Nano 19 (2025) 26400–26410.
[14] T. Li, Z. Xie, W. Zhou, H. Tong, Y. Wu, X. Song, Study on the hydrogen absorption properties of a YGdTbDyHo rare-earth high-entropy alloy, Int. J. Miner. Metall. Mater. 32 (2025) 127–135.
[15] (See, for a review) J. Jensen, A.R. Mackintosh, Rare Earth Magnetism, Clarendon Press, Oxford, U.K., 1991.
[16] A. Takeuchi, A. Inoue, Classification of bulk metallic glasses by atomic size difference, heat of mixing and period of constituent elements and its application to characterization of the main alloying element, Mater. Trans. 46 (2005) 2817–2829.
[17] J.W. Yeh, S.K. Chen, S.J. Lin, J.Y. Gan, T.S. Chin, T.T. Shun, C.H. Tsau, S.Y. Chang, Nanostructured high-entropy alloys with multiple principal elements: Novel alloy design concepts and outcome, Adv. Eng. Mater. 6 (2004) 299–303.
[18] J.W. Yeh, Recent progress in high-entropy alloys, Ann. Chem. Sci. Mat. 31 (2006) 633–648.
[19] B.S. Murthy, J.-W. Yeh, S. Ranganathan, P.P. Bhattacharjee. High-Entropy Alloys, 2nd ed, Elsevier, Amsterdam, The Netherlands, 2019.
[20] Y. Zhang, T.T. Zuo, Z. Tang, M.C. Gao, K.A. Dahmen, P.K. Liaw, Z.P. Lu, Microstructures and properties of high-entropy alloys, Prog. Mater. Sci. 61 (2014) 1–93.
[21] B. Cantor, I.T.H. Chang, P. Knight, A.J.B. Vincent, Microstructural development in equiatomic multicomponent alloys, Mater. Sci. Eng. A 375–377 (2004) 213–218.
[22] K. Ackland, L.M.A. Monzon, M. Venkatesan, J.M.D.Coey Magnetism, of nanostructured CeO_2, IEEE Trans. Magn. 47 (2011) 3509–3512.
[23] J. Luňáček, O. Životský, P. Janoš, M. Došek, A. Chrobak, M. Maryško, J. Buršík, Y. Jiráskova, Structure and magnetic properties of synthesized fine cerium dioxide nanoparticles, J. Alloy. Compd. 753 (2018) 167–175.
[24] F.E. Mabbs, D.J. Machin, Magnetism and Transition Metal Complexes, Chapman and Hall, London, U.K., 1973, p. p7.
[25] G.A. Bain, J.F. Berry, Diamagnetic corrections and Pascal's constants, J. Chem. Educ. 85 (2008) 532–536.
[26] J.A. Mydosh, Spin Glasses: An Experimental Introduction, Taylor & Francis, London, U.K., 1993, p. 67.

[27] T. Kasuya, Electrical resistance of ferromagnetic metals, Prog. Theor. Phys. 16 (1956) 58–63.
[28] M.E. Fisher, J.S. Langer, Resistive anomalies at magnetic critical points, Phys. Rev. Lett. 20 (1968) 665–668.
[29] J. Kudrnovský, V. Drchal, I. Turek, S. Khmelevskyi, J.K. Glasbrenner, K. D. Belashchenko, Spin-disorder resistivity of ferromagnetic metals from first principles: The disordered-local-moment approach, Phys. Rev. B 86 (2012) 144423.
[30] H. Yamada, S. Takada, Negative magnetoresistance of ferromagnetic metals due to spin fluctuations, Prog. Theor. Phys. 48 (1972) 1828–1848.
[31] H. Yamada, S. Takada, Magnetoresistance of antiferromagnetic metals due to *s-d* interaction, J. Phys. Soc. Jpn. 34 (1973) 51–57.
[32] B. Lebech, B.D. Rainford, The magnetic structures of praseodymium and neodymium, J. Phys. Colloq. 32 (C1) (1971) 370–C1-371.
[33] K.A. McEwen, G.J. Cock, L.W. Roeland, A.R. Mackintosh, High-field magnetization of light rare-earth metals, Phys. Rev. Lett. 30 (1973) 287–290.
[34] S.K. Sinha, in: K.A. Gschneidner, L. Eyring (Eds.), Handbook on the Physics and Chemistry of Rare Earths, 1, North Holland, Amsterdam, The Netherlands, 1978, p. 489.
[35] E.P. Gibbons, E.M. Forgan, K.A. McEwen, The magnetic structure of DHCP $Ce_{0.75}Y_{0.25}$ and cerium, J. Phys. F. 17 (1987) L101–L104.
[36] K.A. McEwen, E.M. Forgan, H.B. Stanley, J. Bouillot, D. Fort, Neutron diffraction study of the magnetic structure of neodymium in a magnetic field, Phys. B 130 (1985) 360–362.
[37] E.M. Forgan, E.P. Gibbons, K.A. McEwen, D. Fort, Observation of a quadruple-*q* magnetic structure in neodymium, Phys. Rev. Lett. 62 (1989) 470–473.
[38] W.C. Koehler, R.M. Moon, Magnetic Structures of Samarium, Phys. Rev. Lett. 29 (1972) 1468–1472.
[39] (See, e.g) K. Binder, A.P. Young, Spin glasses: Experimental facts, theoretical concepts, and open questions, Rev. Mod. Phys. 58 (1986) 801–976.
[40] J.M.D. Coey, Magnetism and Magnetic Materials, Cambridge University Press, Cambridge, U.K., 2010, pp. 35–37, 141–143 and 217–218.